Estimating the impact of a 2017 smoke plume on surface climate over northern Canada with a climate model, satellite retrievals, and weather forecasts

Robert D. Field[1,2], Ming Luo[3], Susanne E. Bauer[2], Jonathan E. Hickman[2,4], Gregory S. Elsaesser[1,2], Keren Mezuman[2,4], Marcus van Lier-Walqui[2,4], Kostas Tsigaridis[2,4], Jingbo Wu[1,2]

[1] Department of Applied Physics and Applied Mathematics, Columbia University
[2] NASA Goddard Institute for Space Studies
[3] NASA Jet Propulsion Laboratory
[4] Center for Climate Systems Research, Columbia University

Corresponding author: Robert Field (robert.field@columbia.edu)

Key points

- We captured the overall pattern and magnitude of a large 2017 smoke plume over Canada with the NASA GISS ModelE.
- Higher NO_x emissions, free-tropospheric smoke release and mass-based aerosols led to unrealistically high aerosol optical depth.
- Over an 850 000 km^2 region, we estimated a 16-day surface cooling of between 1.5 ^oC and 4.9 ^oC.

Abstract

In August 2017, a smoke plume from wildfires in British Columbia and the Northwest Territories recirculated and persisted over northern Canada for over two weeks. We compared a full-factorial set of NASA Goddard Institute for Space Studies ModelE simulations of the plume to satellite retrievals of aerosol optical depth and carbon monoxide, finding that ModelE performance was dependent on the model configuration, and more so on the choice of injection height approach, aerosol scheme and biomass burning emissions estimates than to the choice of horizontal winds for nudging. In particular, ModelE simulations with free-tropospheric smoke injection, a mass-based aerosol scheme and high fire NO_x emissions led to unrealistically high aerosol optical depth. Using paired simulations with fire emissions excluded, we estimated that

for 16 days over an 850 000 km^2 region, the smoke decreased planetary boundary layer heights by between 253 m and 547 m, decreased downward shortwave radiation by between 52 Wm^{-2} and 172 Wm^{-2}, and decreased surface temperature by between 1.5 ^{o}C and 4.9 ^{o}C, the latter spanning an independent estimate from operational weather forecasts of a 3.7 ^{o}C cooling. The strongest surface climate effects were for ModelE configurations with more detailed aerosol microphysics that led to a stronger first indirect effect.

Plain Language Summary

Smoke from biomass burning is known to have effects on surface weather. We used the NASA GISS ModelE to estimate these effects for a large 2017 smoke plume over northern Canada that persisted for two weeks. We first found that the height of the smoke release at the source was the most important factor influencing agreement between ModelE and satellite retrievals of aerosols and carbon monoxide, and that specific, plausible configurations of the model led to unrealistically high aerosol amounts. By comparing simulations with and without fire, we estimated a 16-day cooling over a 850 000 km^2 region of between 1.5 ^{o}C and 4.9 ^{o}C, depending on the model configuration.

1. Introduction

The stratospheric smoke plume from Pacific Northwest Event (PNE) wildfires on August 12 and 13 2017 has been studied observationally for its source strength, injection altitude, lifetime, and dynamical effects (Peterson et al., 2018; Torres et al., 2020; Fromm et al., 2021; Lestrelin et al., 2021) and with models to determine the role of 'self-lofting' in its ascent (Yu et al., 2019) and its radiative impacts (Das et al., 2021). At about the same time there was also high fire danger and extensive fire southeast of Great Slave Lake in Northwest Territories (NWT) of Canada (Figure 1) which contributed to the persistent smoke plume (Figure 2) in an otherwise fairly clean environment. Wizenberg et al. (in press) considered both the PNE and NWT emissions at different altitudes in their comparison of chemical transport model simulations to satellite and ground-based trace gas retrievals.

This is a useful natural experiment to evaluate a model against satellite data and to estimate the regional effects of smoke on surface climate. Our study follows basic model-observation

comparisons for, for example, smoke events in Russia (Huijnen et al., 2012; Palacios-Peña et al., 2018; Toll et al., 2015) and North America (Mallet et al., 2017; Lu and Sokolik; Carter et al., 2020). The effects of smoke on surface climate have been examined using discrepancies between operational weather forecasts and observations (Wexler, 1950; Robock, 1988, 1991; Mitchell et al., 2006; Jones et al., 2022) or with models comparing experiments with and without smoke or its radiative effects (Westphal and Toon, 1991; Toll et al., 2015; Walter et al., 2016; Kochanski et al., 2019). By absorbing and scattering incoming shortwave radiation, wildfire smoke can directly and indirectly reduce the amount of radiation reaching the surface, leading to warming of the smoke layer, cooling at the surface, reductions in PBL height, and reductions in horizontal wind speeds.

To evaluate different configurations of the model or understand model uncertainty, modeling studies involve one-at-a-time sensitivity tests for different injection height approaches (Toll et al., 2015; Wizenberg et al., in press), aerosol configurations (Forkel et al., 2015; Palacios-Peña et al., 2018; Konovalov et al., 2020), convective transport (Palacios-Peña et al., 2020) or smoke emissions (Pan et al., 2020; Carter et al., 2020; Lu and Sokolik, 2013), but to the best of our knowledge, not simultaneously. Carter et al. (2020), for example, compared model simulations with different biomass burning emissions estimates, but also mention errors in model optics, background aerosols or clouds in satellite retrievals as other possible sources of discrepancy between their model and satellite data.

The goals of this study were to 1) evaluate the sensitivity of model-satellite agreement for this smoke plume to plausible model configurations of aerosols, emissions, injection height, and transport, identifying any interactions between them using structured experimental design and analysis, and 2) estimate the range of smoke effects at the surface during the event. We also compare estimates of the smoke plume effects on surface temperature to an estimate from an operational weather forecast model.

2. Data and methods

2.1. ModelE experiments

We used the NASA GISS-E2.1-AMIP in CMIP6, referred to throughout as ModelE. The physical parameterizations and satellite era climatology are described in Kelley et al. (2020) and the transient historical simulation (1850 – 2014) in Miller et al. (2014). The horizontal and vertical resolution of the atmospheric component of ModelE is 2° in latitude by 2.5° in longitude with 40 vertical layers extending from the surface to 0.1 hPa near the stratopause. The model was run in AMIP mode with prescribed sea surface temperature (SST) and sea ice fraction during the historical period (Rayner et al., 2003). Horizontal winds are nudged to reanalysis to better capture the observed transport of the smoke plume.

Aerosols and ozone are calculated prognostically using either the One-Moment Aerosol (OMA) or the aerosol microphysical model MATRIX (Multiconfiguration Aerosol TRacker of mIXing state) (Bauer et al., 2020). Both aerosol schemes are coupled to the tropospheric chemistry scheme which includes inorganic chemistry of O_x, NO_x, HO_x, CO, and organic chemistry of CH_4 and higher hydrocarbons using the CBM4 scheme (Gery et al., 1989).

MATRIX (Bauer et al., 2008; Bauer et al., 2010; Bauer and Menon, 2012), is an aerosol microphysics scheme based on the quadrature method of moments. MATRIX represents new particle formation with a binary scheme (Vehkamaki et al., 2002), gas-particle mass transfer, aerosol-phase chemistry, condensational growth, and coagulation within and between particle populations. MATRIX is able to explicitly simulate the mixing state of aerosols (Bauer et al., 2013). The amount of water in aerosol is calculated with the aerosol thermodynamics module EQSAM (Metzger et al., 2002), using the phase state of an ammonia-sulfate-nitrate-water inorganic aerosol in thermodynamic equilibrium for metastable aerosols. As such, hygroscopic swelling of aerosol is represented and does not need to be recalculated during the radiative calculations. Secondary organic aerosol (SOA) is parameterized as a source of non-volatile aerosol emitted directly from vegetation. A 10% yield from monoterpene emissions is assumed, which is added to the non-volatile organic aerosol fraction in the model and remains indistinguishable from organic aerosols from other sources.

OMA (Bauer et al., 2020; Bauer et al., 2007a; Bauer et al., 2007b; Bauer and Koch, 2005; Koch et al., 2006; Miller et al., 2006; Tsigaridis et al., 2013), is a mass-based scheme in which aerosols are externally mixed and (except for sea salt and dust) assumed to have a prescribed constant size distribution. The following aerosol components are treated in this version: sulfate, nitrate, ammonium, carbonaceous aerosols (black carbon and organic carbon, including the NO_x-dependent formation of SOA from isoprene and terpenes) (Tsigaridis and Kanakidou, 2007), methanesulfonic acid formation from dimethyl sulfide, dust (including heterogeneous gas uptake on dust surfaces) (Bauer and Koch, 2005) and sea salt. SOA is formed from isoprene and terpene oxidation. Terpene emissions have a seasonal but not interannual variability and do not respond to climate, while isoprene emissions are calculated prognostically (Guenther et al., 1993), increasing in a warmer climate (Tsigaridis and Kanakidou, 2018) and impacting SOA. Aerosol hydration in OMA is calculated in the radiation code (Tang and Munkelwitz, 1994). The aerosol number concentrations that impact clouds are obtained from the aerosol mass (Menon and Rotstayn, 2006). All aerosol species can activate clouds, including dust in case it is coated with inorganic coatings.

The interactive composition runs, either using MATRIX or OMA, include aerosol-cloud effects, but that only affect cloud optical depth of stratiform and convective clouds. As such we only considered the first (Twomey) indirect effect (Twomey, 1977), and intrinsically via radiation feedbacks semi-direct effects. Anthropogenic fluxes come from the Community Emissions Data System inventory (Hoesly et al., 2018) and sea salt, dimethyl sulfide, isoprene and dust emission fluxes are calculated interactively. All other forcings, such as solar, volcanic (prescribed as stratospheric AOD and aerosol size) and land-use follow the CMIP6 protocol (Eyring et al., 2016).

We considered structural model configuration options for aerosols, biomass burning emissions, injection heights and nudging winds, the choice of which could affect the model's agreement with satellite data and the effects of smoke. We call these options factors, each with two levels, adopting experimental design language. The experiments are listed in Table 1. For the aerosol scheme, we compared OMA to MATRIX. For biomass burning emissions, we compared daily

Global Fire Emissions Database (GFED4s) (Van Der Werf et al., 2017) to the Global Fire Assimilation System (GFASv1.2) (Kaiser et al., 2012) estimates. Either product led to better simulated GEOS-Chem aerosol optical depth (AOD) compared to Moderate Resolution Imaging Spectroradiometer (MODIS) retrievals over North America for 2012 and 2014 compared to other similar emissions products (Carter et al., 2020). In the absence of MODIS Collection 5 burned area for 2017, the GFED4s estimates are a 'beta' version using 2017 MODIS active fire detections and the historical relationship between active fires and burned area. No scaling factors have been applied to either of GFAS or GFED emissions.

For injection height, we compared the standard ModelE approach of distributing smoke emissions evenly through the planetary boundary layer to prescribed but variable daily-mean injection heights from offline estimates from GFAS that account for the effects of fire radiative power on plume buoyancy (Remy et al., 2017). The latter approach allows for the release of smoke into the free troposphere for higher intensity fires. Wizenberg et al. (in press) used the GFAS 'mean altitude of maximum injection' for their GEOS-Chem simulations as a baseline against which other injection heights were tested. We instead used the GFAS 'altitude of plume top' parameter which tended to be higher in altitude. For nudging of 6-hourly horizontal winds, we compared National Center for Environmental Prediction (NCEP) (Kalnay et al., 1996) to Modern-Era Retrospective Reanalysis 2 (MERRA2) (Gelaro et al., 2017) reanalysis fields.

We used a full-factorial experimental design (Sexton et al., 2003; Montgomery, 2013) with $2^4 = 16$ simulations to test all combinations of the four factors with two levels each. In Table 1, the four-letter AEIW code at the end of each experiment label indicates the factor levels: (O)MA or (M)ATRIX aerosols, GFA(S) or GFE(D) biomass burning emissions, (P)BL or (V)ARIABLE injection height, and (M)ERRA2 or (N)CEP winds.

2.2. Satellite retrievals

We evaluated ModelE against L2 AOD retrievals from MODIS instruments on board Terra and Aqua and L2 carbon monoxide (CO) retrievals from the Measurements of Pollution in the Troposphere (MOPITT) instrument on board Terra and the Atmospheric Infrared Sounder (AIRS) instrument on board Aqua. Level 3 (L3) satellite sounder temperature retrievals from

instruments on Suomi National Polar-orbiting Partnership (S-NPP) are used for understanding impact on atmospheric thermal structure.

Moderate Resolution Imaging Spectroradiometer (MODIS) sensors measure radiance in 36 spectral bands ranging from 0.41 to 14.2 μm over swaths of 2,300 km (2-day global coverage). We use MODIS AOD at 550nm obtained by merging Dark Target and Deep Blue retrievals (Sayer et al., 2014) from the from 10x10 km Collection 6.1 L2 gridded products MOD04_L2 and MYD04_L2 (Hubanks et al., 2019). MOPITT is a gas-correlation instrument that provides synoptic coverage of CO concentrations every 3 days, with a footprint size of 22 km at the nadir. Its thermal infrared and near infrared retrieved v7 CO data (Deeter et al., 2017) provide sensitivities in the lower troposphere in addition to the maximum sensitivity in the middle troposphere from thermal infrared-only retrievals. AIRS is a 2,300-channel infrared grating spectrometer in a sun-synchronous orbit with northward equator crossing time of 1:30 PM. AIRS CO is retrieved with horizontal resolution of 45 km at nadir, in a swath of width 30 field-of-views or about 1,600 km. This orbit gives global coverage in the tropics every 2 days. The retrieval uses a cloud clearing methodology providing CO with sensitivity that peaks around 500 hPa, with ~0.8–1.2 degrees of freedom of signal for 50–70% of scenes. More sampling and higher information content are obtained in clear scenes (Warner et al., 2013).

L3 temperature profile retrievals (~45 km horizontal spatial resolution, on standard pressure levels) from the Community Long-term Infrared Microwave Combined Atmospheric Processing System algorithm (Smith and Barnet, 2019, 2020) applied to the S-NPP Cross-track Infrared and Microwave Sounding Suite (CrIMSS) platform (with nearly identical orbital characteristics as Aqua/AIRS) are used for quantifying domain mean thermal structures temporally and spatially co-located with the main plume. Smith and Barnet (2020) provide extensive discussion on uncertainty, with the cloud clearing approach and use of microwave radiances in the retrieval ensuring that temperature retrievals above the lowest portion of the boundary layer are robust to contamination by the plume and potential clouds.

The L2 satellite data were compared to instrument-equivalent hourly ModelE fields. This involved orbital collocation, masking model fields according to retrieval quality, and coarsening

the satellite retrievals to the 2° x 2.5° ModelE grid. For MODIS and AIRS, model fields were collocated to 5 and 6-minute L2 scenes respectively and interpolated to the 10km pixel level. Individual, interpolated model pixels were masked out where retrievals were unsuccessful due to clouds or thick smoke being flagged as clouds. ModelE AOD values greater than 5.0 were set to 5.0, the maximum possible MODIS retrieval value. The satellite CO profile retrievals are the optimal estimates of the species concentrations combining information from the measured nadir radiances and the a priori knowledge of the profiles. The retrieval system operator therefore needs to be applied to the model CO profiles for proper comparisons to the satellite CO profile retrievals explained in detail by Luo et al. (submitted) for satellite data applications. For AIRS, application of the averaging kernel involves a trapezoidal component as part of the convolution (McMillan et al., 2011; Kopacz et al., 2010). CO was analyzed in the mid-troposphere between 300 and 600 hPa, where both MOPITT and AIRS retrievals both have their greatest sensitivity. The bias, RMSE and spatial pattern correlation over 50N-80N, 140W to 30W between each model ensemble member and the satellite data was calculated, similar to Pere et al. (2014) during the main plume period of August 12-27 to evaluate model-satellite agreement. The temporal evolution of the modeled AOD and CO under the most persistent part of the plume was compared to the satellite retrievals.

The sensitivity of model-satellite agreement to the four factors and their interactions was estimated using a regression analysis of the factorial design:

$$Y = b_0 + b_1 A + b_2 E + b_3 I + b_4 W + \\ + b_5 AE + b_6 AI + b_7 AW + b_8 EI + b_9 EW + b_{10} IW + \varepsilon \quad (1)$$

where the response Y is the bias, RMSE or pattern correlation between model and satellite data. A (aerosols), E (emissions), I (injection height), and W (winds) are -1/1 variables. For aerosols (A:b_1), OMA is coded as -1 and MATRIX is coded as 1. For emissions (E:b_2) GFAS is coded as -1 and GFED is coded as 1. For injection height (I:b_3), PBL is coded as -1 and VARIABLE is coded as 1. For winds (W:b_4), NCEP is coded as -1 and MERRA2 is coded as 1. The coefficients b_1-b_4 are for the main effects, b_5-b_{10} are for the 2-factor interactions, and ε is the residual error term. By interaction, we mean, for example, whether the relative performance of one aerosol module over the other depends on the choice of emissions. The strength and significance of the estimated coefficients indicate the influence of each main effect or interaction on different Y

response variables and the main effects are calculated as $2*b_i$. We refer to Montgomery (2013) for further details on the factorial design and analysis.

2.3. Estimates of smoke effects on surface climate

Each experiment in Table 1 was run with fire emissions over western North America removed. Smoke effects on short-wave downward solar radiation (SWDS), planetary boundary layer (PBL) height, 2m surface temperature and vertical temperature were estimated from the difference between each pair of fire and no-fire simulations over a smaller region in northern Canada where the observed plume, on average, had the highest CO and AOD concentrations over August 12-27. The regression model in (1) was also used to estimate the importance of each of the four factors on surface climate.

As an independent comparison against the GCM results, we also examined forecast-observation discrepancies under the thickest part of plume, following the approach of Robock (1991) and Mitchell et al. (2006), and also accounting for any systematic forecast biases. We used 24-hour forecasts of daily maximum 2m temperature from the NOAA National Centers for Environmental Prediction Global Forecast System (GFS). Because fire and smoke are not included in GFS, the difference between the forecast and the observations provides an estimate, indirectly, of the smoke effects after accounting for the background forecast bias. Forecasts were compared to observations from 10 weather stations from the National Centers for Environmental Information (NCEI) Integrated Surface Database (ISD) (Smith et al., 2011). Station data was filtered using the ISD quality control codes and spatially interpolated to the GFS grid. Forecasts were compared to individual station data and to the regional average over land from the interpolated data.

3. Results

3.1. Emissions and satellite retrievals of plume

Figure 3 shows the daily GFAS and GFED estimates for three representative constituents. GFAS and GFED emissions are similar for CO (Figure 3a), significantly different for NO_x (Figure 3b), and somewhat different for black carbon (BC, Figure 3b). The bulk of the emissions for this episode were from August 13-15, in contrast to the 2010 Russian fire episode where emissions

268 persisted variably from mid-July through mid-August. In terms of total emissions amounts,
269 Huijnen et al. (2012) estimated 12Tg CO emissions from an earlier version of GFAS for the 1-
270 month Russian smoke episode compared to 5.8 and 5.3 Tg from GFAS and GFED respectively
271 for Aug 11-15 in Figure 3. The GFAS injection heights for the VARIABLE experiments in Table
272 1 ranged from 3.5 km to 4.5 km during August 13-15, compared to average PBL heights of 1km
273 for the experiments.
274
275 Figure 4 shows the average MODIS AOD, and mid-tropospheric CO from MOPITT and AIRS
276 over August 12 to August 27, with the number of days with valid retrievals for each product.
277 MODIS AOD (Figure 4a) has prominent features over the western Canadian Arctic islands, over
278 the southern Arctic northwest of Hudson's Bay, and over the north Atlantic. Individual grid cells
279 with high (>2) average AOD are based on a small number of retrievals (Figure 4b). The
280 MOPITT CO enhancement (Figure 4c) extends from James Bay to the high Artic, with retrieval
281 quality generally decreasing northward (Figure 4d), with individual high (> 300 ppb) CO grid
282 cells calculated from few retrievals. There is higher MOPITT CO over the north Atlantic, but
283 which is also based on fewer retrievals. The AIRS CO (Figure 4e) shows a similar pattern to the
284 MOPITT CO but is smoother and lacks the enhancement in the high Arctic. The AIRS CO
285 average is based on more retrievals over this period (Figure 4f) because of its spatial
286 interpolation approach.
287
288 For each satellite retrieval, the August 12-27 average reflects the initial high smoke
289 concentration in southern Nunavut followed by the plume splitting around a center of low
290 pressure over Baffin Bay on August 17. The southern plume segment traveled over the north
291 Atlantic. The northern segment of the plume traveled northward over the Arctic Ocean and
292 northern Greenland and was then recirculated southward from August 20 to 24 before dispersing
293 over northern Ontario, like the recirculation of smoke during the 2010 episode in Russia (Witte
294 et al., 2011; Pere et al., 2015; Pere et al., 2014). MOPITT CO on August 19 (not shown) closely
295 matches the IASI column CO for that day from Wizenberg et al. (in press), with a CO
296 enhancement stretching from northern Greenland southwestward around a center of low pressure
297 to Hudson's Bay and a second enhancement off the southern tip of Greenland.

3.2. Model-satellite comparison

Figure 5 shows the difference between the ModelE and MODIS AOD in Figure 4a for the 16 simulations in Table 1. The bias, RMSE and pattern correlation between ModelE AOD and the MODIS AOD over the large magenta box are listed in each panel caption and summarized in Table 2. The retrieval quality in Figure 4b is accounted for in the comparisons through the masking step in estimating the instrument-equivalent model fields.

All simulations show a mix of regional positive and negative AOD biases in ModelE, with most having an overall negative bias over the whole domain and the Arctic islands, and each having a negative bias over the north Atlantic plume segment. Over the persistent part of the plume northwest of Hudson's Bay shown by the small blue box, there are mostly positive biases of different magnitudes. The strong positive biases for experiments 05_OSVM (Figure 5e) and 13_OSVN (Figure 5m) extend over the Arctic islands and contribute to those experiments having RMSE (0.48 and 0.52 respectively) well outside of the range (0.32-0.39) of other experiments (Table 2). As an indication of the magnitude of the smoke plume, experiments where biomass burning over western North America were removed had AOD biases ranging from -0.37 to -0.32, and RMSE of 0.54 to 0.57. The pattern correlation ranged from -0.04 to 0.15, compared to between 0.61 and 0.75 for experiments with smoke emissions.

Figure 6 shows the difference between the ModelE and MOPITT CO in Figure 4b. Like the AOD, the model CO has a mix of regional positive and negative biases. The strongest biases are positive for experiments 5-8 (Figure 6e-h) extending from Hudson's Bay to northwest Greenland, and secondarily for experiments 13-16 (Figure 6m-h), which had in common variable injection heights. For experiments with smoke released through the PBL (Figure 6a-d & m-p), the biases over the main plume region were generally weaker and negative. Figure 7 shows the difference between the ModelE and AIRS CO in Figure 4c. The Model has similar but smoother and weaker biases relative to AIRS CO compared to MOPITT CO.

Figure 8 shows the time-evolution of the modeled AOD and CO over the main persistent plume region for each experiment and the satellite retrievals. All ModelE AOD peaks between values of 1.6 and 3.6 one day earlier than the MODIS AOD peak of 2.3 on August 15, capturing to varying

degrees a secondary MODIS increase to 1.7 on August 17 and decreasing steadily afterward (Figure 8a). The exceptions are the 05_OSVM and 13_OSVN experiments which for August 17-24 are a twice as high as MODIS AOD. There was a similar, smaller AOD enhancement for these experiments August 5-6. The modeled CO also peaks earlier than the MOPITT peak of 254 ppbv (Figure 8b) for configurations with variable injection heights and generally remains flat for simulations with PBL release. Most configurations overestimate CO during the secondary MOPITT peak of 193 ppbv on August 21. Comparisons to AIRS were similar (Figure 8c). Across all experiments, there was no obvious 'best' model configuration.

3.3. Contributions of aerosols, emissions, injection height and winds to model-satellite comparisons

The regression estimates for Model vs. MODIS AOD are shown in Table 3. These quantify the influence of each factor on the model-satellite agreement metrics in Table 2, and the 2nd order interactions between each factor; we focus on the regression estimates for the bias. The choice of aerosols, emissions, and injection height significantly affected model the bias, whereas the choice of nudging winds did not. The AOD model bias is more negative for MATRIX relative to OMA (b_1=-0.036), which is equal to half the difference between the average AOD bias in Table 2 across all OMA experiments (-0.003) and the average bias across all MATRIX experiments (-0.074). Although the choice of aerosol module had a significant effect on the bias, it did not have a significant effect on the RMSE. For the emissions, the model AOD bias decreased for GFED relative to GFAS (b_2=-0.054), which represents an increase in magnitude, but decreased the RMSE marginally. The injection height choice had a slightly greater effect on the bias (b_3=0.056) and RMSE compared to the emissions, with variable injection heights having a higher bias and RMSE compared to PBL injection. The choice of winds only had a significant effect on the spatial pattern correlation (b_4=-0.037), which was lower for NCEP compared to MERRA2, and also interacted with injection height (b_{10}=0.011).

The interaction effect between aerosols and emissions (b_5= 0.032) was smaller than the emissions or injection height main effects, but comparable in magnitude to the main aerosol module effect. This can be interpreted using the interaction plots in Figure 9, described in detail in Montgomery (2013). In each panel, significant interactions are present when the slopes of the

two lines are different. For the aerosol-emissions interaction in the first row and second column, the model AOD bias is insensitive to the emissions when MATRIX aerosols are used (Aerosols=M, green dotted line), but for OMA aerosols (Aerosols=O), the AOD bias is significantly higher for GFAS (Emissions=S) compared to GFED (Emissions=D). These estimates are strongly influenced by the high bias of experiments 05_OSVM and 13_OSVN (Table 2) which had OMA aerosols, GFAS emissions, and variable injection heights. There was also a significant interaction effect between emissions and injection height (b_8= -0.018), but as can be seen in the interaction plot, it was weaker. This contrasts with the interactions between winds and the other three factors, where the slopes for all interactions are similar.

The bias between MOPITT and model CO (Table 4) was significantly influenced by injection height (b_3=5.5) and to a lesser degree by winds (b_3=-1.3). For the coding of PBL=-1, and VARIABLE=1, the interpretation is that variable injection heights had a bias of 11.0 (=2*b_3) ppbv higher than for smoke released into the PBL. This quantifies in a more objective sense the groupings in Table 2 and Figure 6, which showed a group of lower bias (and RMSE) simulations with PBL release (01-04, 09-12) and higher bias simulations (05-08, 13-16) with variable injection. There were no significant interactions between the factors, and the main wind effect, while significant, was relatively small. The bias between AIRS CO and model CO (Table 5) was also influenced by injection height (b_3=4.3), and to lesser degrees by the aerosol scheme (b_1=2.8), emissions (b_2=-0.8) and winds (b_4=-0.7). There was also a significant but small interaction between aerosol scheme and injection height (b_6=2.6).

3.4. Smoke effects on surface climate

3.4.1. ModelE

The daily maximum solar downward shortwave radiation at surface (SWDS) across ensemble members with difference between fire and no-fire experiments is shown in Figure 10. This is over the ~850,000 km^2 land area in the blue box in the maps. From July 1 to August 11 there are two MERRA2 and NCEP groups in the experiments, but otherwise little variation in downward shortwave at the surface (Figure 10a). There is considerable variation across simulations from August 12-27 when the plume is present (Figure 8). Figure 10b shows the difference between the experiments with fire and without fire for each experiment, which isolates smoke effects. During

the main plume period, there is a wide range of effects of smoke across members. On August 14th, for example, the effects of the smoke ranged from -122 Wm^{-2} for 11_ODPN to -357 Wm^{-2} for 14_MSVN.

The daily maximum planetary boundary layer heights across ensemble members are shown in Figure 11. There is more variability in PBL height prior to the smoke plume (Figure 11a) compared to incoming solar radiation, with higher PBLs for the MERRA2-nudged winds than the NCEP-nudged winds. Decreases in PBL between fire and no-fire experiments (Figure 11b) ranged from 600m to 1200m on August 14th. The daily maximum surface temperature across ensemble members is shown in Figure 12. There was a similar MERRA2/NCEP grouping of experiments prior to the smoke plume arriving on August 12 (Figure 12a), caused by the differences in the large-scale circulation and transport imposed by the nudging and any consequent responses from the subgrid parameterizations. The effects of the smoke on surface temperature (Figure 12b) had a spread comparable to that in the SWDS. On August 14th the smoke effects on daily maximum surface temperature ranged from -4 ºC for experiments 03_ODPM and #11 with OMA aerosols, GFED emissions and PBL injection to -11ºC for 14_MSVN with MATRIX aerosols, GFAS emissions and variable injection heights.
Figure 13 shows the change in the vertical temperature profile over the same region and period. The grouping of experiments with the strongest temperature decreases at the surface in Figure 12b corresponds to the strongest warming in the mid troposphere between 200 and 600 hPa. These had MATRIX aerosols and variable injection heights and of these, the experiments with GFAS emissions (06_MSVM, 14_MSVN) had the strongest vertical temperature response.

Table 6 summarizes average surface climate effects over August 12-27 for each experiment. Excluding experiments 05_OSVM and 13_OSVN which had outlying AOD bias and RMSE, the time-averaged smoke effect on SWDS ranged from -53 Wm^{-2} to -172 Wm^{-2}, on PBL height ranged from -253 m to -547 m, and on surface temperature from -1.4 ºC to -4.9 ºC. The variation in smoke effects on SWDS could explain 95% of the variation in surface temperature effects and 94% in PBL effects.

Table 7 shows the regression estimates of the factor effects on SWDS, PBL and surface temperature changes in Table 6. The effect of smoke on SWDS was most strongly affected by the choice of aerosol scheme (b_1=-28.6), where MATRIX aerosols, on average, reduced the SWDS by 57.1 Wm^{-2} (=2*b_1) more than OMA. The choice of injection height (b_3=-15.5) and emissions (b_2 = 9.3) also had effects, with variable injection heights reduced SWDS by 31 Wm^{-2} more than PBL release, and GFAS by 18.6 Wm^{-2} less than GFED. The choice of nudging winds did not have a significant effect on its own but did interact with the choice of injection height, although the effect (b_{10}=-4.5) was small compared to the main effects. The effect of smoke on the PBL height was also most strongly affected by the choice of aerosols (b_1=-70.6), and next by the injection height (b_3=-47.8) and emissions (b_2=22.4). Similarly, the effect of smoke on the surface temperature was most strongly affected by the choice of aerosols (b_1=-0.75), and next by the injection height (b_3=-0.6) and emissions (b_2=-0.309). In summary, SWDS, PBL height and surface temperature were affected by, in decreasing order, the choice of aerosol scheme, the injection height approach, and the emissions, and were strongest for MATRIX aerosols, GFAS emissions and variable injection heights.

3.4.2. GFS forecasts and temperature observations

The daily maximum surface temperature for 10 surface weather stations and 24-hour GFS forecasts are shown in Figure 14. During the mid-August smoke plume period shown by the grey shading, the forecasts over Bathurst Inlet, Baker Lake, Arviat, Whale Cove Airport, Rankin Inlet, Chesterfield Inlet and perhaps Wager Bay appear to show a warm forecast bias outside of the background forecast discrepancies. The discrepancies must be accounted for in any quantitative estimate of smoke effects and are estimated during the July 1 to August 11 pre-plume period. These are summarized in Table 8, along with the bias during the plume period. The effect of the smoke is estimated as the difference between the two periods. Averaged over August 12-27, the smoke effect ranges from -2.0 °C at Coral Harbour on Southampton Island to -5.8 °C at Whale Cove Airport. The estimated smoke effects are mapped in Figure 15.

Figure 16 shows the daily GFS-estimated bias in forecast temperature and the ModelE fire – no-fire difference across 14 ‘permissible’ experiments (all but 05_OSVM and 13_OSVN) for July and August 2017. Pre-plume, the GFS forecast had an average bias of -1.5 °C in daily maximum

temperature relative to the weather station temperatures interpolated to the GFS grid. The bias was 2.2 ºC over August 12-27 (and significant according to a t-test), with forecasts being too warm because they do not account for the smoke and its surface cooling effects. This suggests an average GFS-estimated smoke effect of -3.7 ºC, which reached a minimum of -6.4 ºC on August 15. The average ModelE fire – no-fire temperature difference averaged over the permissible ensemble subset is shown by the magenta line. Over August 12-27, the average temperature effect over this subset was -3.0 ºC, which reached a minimum of -6.8 ºC on August 14. The ModelE temperature decrease leads that estimated from GFS by a day, which is consistent with the earlier peak in modeled AOD across most ensemble members compared to MODIS (Figure 8a).

Figure 17 shows the temperature anomalies for CrIMSS and radiosonde profiles at Baker Lake, listed station #3 in Table 8, which has some missing data in mid-July. For both datasets, the July-August 2017 average profile has been subtracted from the daily CrIMSS profiles and the 12-hourly sonde profiles. There is a unique positive tropospheric temperature anomaly in the CrIMSS profile from August 12-17 and more weakly from August 24-27 with corresponding negative temperature anomalies at the tropopause (Figure 17a). Part of this feature is driven by the background meteorology (i.e. a heat dome), but the overall pattern is consistent with the vertical temperature changes in ModelE (Figure 13) that are due only to smoke effects. The same features appear in the Baker Lake radiosonde profile (Figure 17b), but more clearly than the CrIMSS profiles which have limited vertical resolution, particularly an issue for resolving the temperature structure in the lower troposphere and boundary layer. The negative anomaly from the surface to 900 hPa in the sonde profile is consistent with the estimated 2m surface cooling estimated at Baker Lake (Table 8) and appears only weakly in the CrIMSS profile owing to its limited sensitivity near the surface. Overall, with ModelE and observed surface temperature data suggesting cooling at the surface, and the model, radiosonde and satellite soundings suggesting warming in the free troposphere, there is a resultant increase in tropospheric stability, which, superposed on an existing heat dome, would inhibit tropospheric overturning and convective processes (and precipitation).

4. Discussion

The agreement between ModelE simulations of the smoke plume and satellite data were dependent on which configuration of the model was used, as were the estimated effects of smoke on surface climate. The use of prescribed, variable injection heights increased the model AOD relative to MODIS. This was also the case for model CO relative to MOPITT and AIRS because of longer smoke lifetimes in the free troposphere compared to releasing smoke through the boundary layer, although this could be sensitive to our comparison over the mid-free troposphere where the MOPITT and AIRS have the most sensitivity.

MATRIX aerosols led to lower AOD, as did GFED emissions, but there was a significant interaction effect between the choice of aerosols and emissions. When MATRIX is used, GFAS and GFED had comparable biases. When OMA is used, GFAS had higher positive biases than GFED, driven by the two outlying experiments (05_OSVM and 13_OSVN) with variable injection heights. Modeled CO was insensitive to the choice of emissions because GFAS and GFED CO were so similar for this case (Figure 3a). Compared to MERRA2, nudging with NCEP winds decreased CO relative to MOPITT and AIRS, but overall, the impact of the choice of winds was small compared to the other three factors. Evaluation against the satellite data was more useful in identifying simulations with lower agreement, particularly 05_OSVM and 13_OSVN (OMA aerosols, GFAS emissions and variable injection heights) than in identifying a single 'best' model configuration.

4.1. Explaining the large positive AOD bias for outlier simulations and large surface effects for MATRIX

To explain the large difference in AOD in 05_OSVM and 13_OSVN compared to all other experiments, we looked at the difference in chemical composition in the smoke plume in experiments 01_OSPM, 02_MSPM, 05_OSVM and 06_MSVM, using the average August 2017 speciated AOD available as model output. In the OMA model, when GFAS emissions are emitted through the PBL, the AOD plume in 01_OSPM is attributed to 67% organic aerosol, 16% ammonium-nitrate, 8% sulfate and 7% black carbon, and the remaining 2% are attributed to dust and sea salt. In the variable injection height experiment (05_OSVM) that is otherwise configured the same, the overall AOD increases, and so do all individual chemical components,

but in addition the relative contribution by chemical species changes as well. Most strikingly, ammonium-nitrate contributions increase to 26%, while the other three components' relative contribution decrease, to 59% organic aerosol, 6% sulfate and 6% black carbon.

Overall, this behavior is not surprising considering that higher altitude emissions lead to longer lifetimes of aerosol species and their gaseous precursors, as dry and wet removal processes are less effective if particles are higher above the surface and above clouds. In addition to removal, aerosol chemical production of secondary aerosol is impacted as well. In experiment 05_OSVM ammonium nitrate is especially sensitive to emission height and higher NO_x emission, a precursor for nitrate aerosol, from the GFAS inventory and strongly impacts nitrate formation.

In contrast to the OMA model, the MATRIX model shows less sensitivity to differences in emissions and injection height. In 02_MSPM, AOD is attributed to 81% organic aerosol, 11% sulfate, 4% ammonium-nitrate and 3% black carbon. In experiment 06_MSVM the overall AOD increases as well, but the individual breakdown in components changes much less compared to OMA. The ammonium-nitrates contribution increases to 8%, and organic aerosols are reduced to 78%. Thus there is an overall much-reduced response in nitrate AOD as well as overall contribution to AOD.

MATRIX and OMA differ greatly from each other, and details about the schemes as well as performance are discussed in Bauer et al. (2020). But relevant mechanisms behind the different behaviors could be rooted in the fact that overall sulfate loads in MATRIX are higher compared to OMA, which leads to less nitrate production rates in MATRIX, due to less availability of ammonia. Another important difference between the models is that OMA considers primary as well as secondary production of organic aerosols, and as such aerosol production might be more sensitive to emission height due to the temperature dependence of the vapor pressure of the semi-volatile SOA gaseous precursors. In MATRIX all organic aerosol is treated as primary, including SOA (Section 2.1). MATRIX is a microphysical aerosol model in which the optical properties of aerosols depend on the simulated aerosol sizes and mixing states, while OMA's AOD calculation only depends on the simulated masses of the aerosol species and hydration.

In addition to OMA and variable injection heights, the anomalously high AOD for experiments 05_OSVM and 13_OSVN was also because of higher NO_x emissions for GFAS. The higher NO_x emissions for GFAS than GFED compared to other constituents, in turn, are mainly because of the different emissions factors used in each. For boreal forests, the NO_x emissions factor is 3.4 g/kg for GFAS (Kaiser et al., 2012) and 0.9 g/kg for GFED (Van Der Werf et al., 2017), compared to CO emissions factors of 106 g/kg for GFAS and 127 g/kg for GFED. Inspection of the CO and NO_x emission on August 14 southeast of Great Slave Lake (not shown) suggests contributions from peat burning in GFAS that are absent in GFED, which would further increase the difference between GFAS and GFED NO_x emissions and offset the lower CO emissions factor for GFAS compared to GFED.

The two outlying 05_OSVM and 13_OSVN experiments did not have anomalous surface climate effects despite their higher AOD. In terms of surface effects, the more apparent grouping of experiments all had MATRIX aerosols and variable injection heights, despite not having anomalously high AOD. We attribute this to indirect effects. Figure 18 shows the daily effects of smoke on maximum cloud optical depth over the small plume region. The experiments 06_MSVM, 08_MDVM, 14_MSVN, 16_MDVN with the greatest fire-no fire difference in cloud optical depth (Figure 17b) correspond to those with the greatest decrease in SWDS (Figure 10b) and surface temperature (Figure 12b). This suggests a stronger first indirect effect for MATRIX compared to OMA when higher injection heights contributed to longer aerosol lifetimes, greater aging, increase in the number of CCN, and a stronger first indirect effect.

4.2. ModelE biases in atmospheric composition compared to other studies

We found a mix of positive and negative biases spatially and temporally compared to satellite AOD and CO that depended on the ModelE configuration. This contrasts with other studies at mid and high latitudes, where smoke-related model biases are mostly low, sometimes high, but typically biased in the same direction, and which tend to focus on a narrower set of model configurations. For the same 2017 event, Wizenberg et al. (in press) found a strong dependence on modeled CO to both injection height and the observations used for comparison. Their default injection closer to the surface led to a strong low bias downwind compared to satellite and ground-based retrievals, whereas an injection height of 5km for the NWT fires led to the best

agreement with IASI column CO over Ellesmere Island, and a 10km injection height led to the best agreement with ground-based column CO retrievals, noting that the 10km injection height was possibly compensating for transport errors.

The best-studied event is the 2010 smoke episode over Russia. Huijnen et al.'s (2012) experiment with an earlier version of GFAS and without assimilation of trace gas retrievals had an overall high negative bias in column CO compared to MOPITT over 3 weeks, particularly over the source region. These were attributed to missing emissions and other model deficiencies. AOD for this experiment agreed well with retrieved AERONET values at Moscow after scaling up direct aerosol emissions by a factor of three. Using a different chemical transport model but the same GFAS emissions as Huijnen et al. (2012) and FRP-driven injection heights, simulated AOD over eastern Europe was biased low relative to MODIS AOD and AERONET AOD at Moscow (Pere et al., 2015), but qualitatively high compared to POLDER AOD (Pere et al., 2014), with discrepancies attributed to transport errors. Toll et al. (2015) found underestimated model AOD relative to MODIS downwind of the source region for a single time step using a different model with prognostic injection heights. This was attributed to lack of SOA formation and hygroscopic growth, and overestimated wet deposition, despite possibly overestimated aerosol emissions but which was improved most straightforwardly by changing the allowable aerosol size distribution, and with effects either way from prognostic injection heights. Across multiple models, underestimated AOD over 3 weeks relative to MODIS was attributed to too-low injection heights (Palacios-Peña et al., 2018). In a follow up study with one of the models (Palacios-Peña et al., 2020), AOD increased or decreased relative to a base case for sensitivity tests to microphysical dependence on relative humidity, dry deposition, wet scavenging and subgrid convective aerosol transport, and often with near-source changes of one sign offset by opposite changes downwind.

In other cases, differences in modeled AOD have also been attributed to a similarly wide range of model components. Hodzic et al. (2007) compared 5 days of simulated to MODIS AOD over Europe in during the August 2003 heat wave, finding improvements with varying smoke injection height and hourly emissions in simulations of large fire events when evaluated against surface and satellite retrievals. Studying smoke plumes from the large 2008 California fires,

Mallet et al. (2017) found good pattern agreement over 6 days but underestimated AOD relative to MODIS and OMI despite scaling up organic carbon emissions by a factor of two to account for the absence of SOA formation. We note that emissions were released only in the lowest layer of their model, which could have also contributed to the underestimated AOD, similar to the lower AOD for emissions released through the PBL in our experiments. Surface release of smoke emissions could have also contributed to underestimated surface PM2.5 and AOD in simulations of a 1-week smoke period in 2007 over Idaho (Jiang et al., 2012). Lu and Sokolik (2013) simulated a large 3-day smoke plume over northern Canada with a high resolution, plume-rise enabled chemical transport model, and found considerable low AOD biases compared to MODIS and OMI without increasing their bottom-up emissions estimates, suspected to be too low because of underestimated burned area. Yu et al. (2016) attributed underestimated AOD near the source in their model relative to MODIS during the 2013 Rim fire to underestimated emissions and coarse model resolution. In their study of a short-lived 2010 smoke plume also over northern Canada, Walter et al. (2016) found the best hourly AOD agreement with a downwind AERONET site for GFAS-driven simulations with a variable injection height model, but which had a slight high bias.

Over the central US and southern Mexico, lower AOD during the spring of 2009 compared to two different MODIS-assimilated products was attributed to underestimated emissions for simulations that used the GFED3 and GFED4 products, while a simulation with QFED generated high biases in surface concentrations compared to IMPROVE network, but were diluted in the AOD, likely due to discrepancies in the smoke's injection height (Liu et al., 2018). Pan et al. (2020) found comparable performance between GEOS simulations with GFAS and GFED4s emissions. The AOD of both were biased slightly high overall compared to MISR over boreal North America in September 2008 and compared to an AERONET site south of Great Slave Lake throughout the year, opposite the more coherent and stronger low biases seen at lower latitudes, and despite smoke being released within the boundary layer and without SOA formation in the host model and possible uncertainty in calculating its AOD. For the full 2012 and 2014 fire seasons over North America, Carter et al. (2020) found that GEOS-Chem AOD was biased low compared to Aqua MODIS AOD over North America, but that GFAS and GFED performed better compared to two other emissions inventories, with the possibility for one

because emissions had been increased to compensate for biases in the aerosol module of its host model, and that for all simulations, too-low injection heights were also a possible contributor to low AOD.

In previous studies, sensitivity tests were mostly done in a one-at-a-time sense by identifying departures from a base case, or, in the case of emissions, scaling them upward to achieve better agreement with observations. Using our experimental design, we compared the relative importance of different model components, finding that between AOD and CO, the choice of injection height scheme had the greatest effect on the model's agreement with satellite retrievals over the large domain. For AOD, the choice of aerosol scheme and emissions was important, as were their interaction with injection height scheme. In a model-development sense, for example, incorporating the variable injection heights with the GFAS emissions and OMA aerosols would suggest a significant degradation in model performance. This would not necessarily be the case with either GFED emissions or MATRIX aerosols, however, and that the more likely cause is high NO_x emissions in that region for the GFAS estimate, which trace back in large part to the emissions factors in Andreae and Merlet (2001).

4.3. Surface effects compared to other events

Surface climate over the main plume region was affected most by the choice of aerosol scheme, with more significant effects for MATRIX compared to OMA, and to lesser degrees by using variable injection heights and GFAS emissions. Across the permissible experiments for August 12-27, the smoke decreased daily maximum incoming solar radiation by between 52 Wm^{-2} and 172 Wm^{-2}, decreased the boundary layer height by between 253 m and 547 m, and decreased the surface temperature by between 1.5 ^{o}C and 4.9 ^{o}C. Our independent estimate of the surface temperature change from discrepancies between the GFS forecast and surface observations was a 3.7 ^{o}C cooling, falling near the middle of the ModelE experiments.

Our estimates of surface climate impacts of the smoke were in line with previous studies, to the extent that they can be compared when over different-sized areas, different periods of time, and using models and observations in different ways. Reductions in shortwave radiation reaching the surface have been estimated in temperate and boreal regions and are comparable in magnitude to

those in our simulations, frequently of the magnitude of ~100 W m^{-2} but ranging from roughly 60 to 600 W m^{-2}. Smoke from wildfires in Russia in 2010 led to reductions SW radiation of 60 to 150 W m^{-2} (Chubarova et al., 2012; Pere et al., 2014; Forkel et al., 2015; Kong et al., 2015; Gleeson et al., 2016; Baro et al., 2017). Different North American fires led to estimated reductions of ~80 W m^{-2} (Fu et al., 2018), >100 W m^{-2} over California in September 2020 (Huang et al., 2023), ~110 W m^{-2} in 2007 over Idaho and Montana (Jiang et al., 2012), nearly 600 W m^{-2} over California in 2015 (Kochanski et al., 2019), ~125 W m^{-2} over CONUS (Juliano et al., 2022), 400 W m^{-2} over Colorado in 2010 (Stone et al., 2011), ~400 W m^{-2} over southern British Columbia (Mckendry et al., 2019), and 300 W m^{-2} over central boreal Canada (Walter et al., 2016). Dimming has also been documented for fires in Australia with reductions of up to 500 W m^{-2} (Mitchell et al., 2006), and in Siberia and China, with reductions of ~60 to 80 W m^{-2} (Fu et al., 2018). Estimates of the dependency of surface radiation on AOD range from roughly 20 to 30 W m^{-2} per unit change in AOD (Fu et al., 2018; Santos et al., 2008) and as high as 120 to 140 W m^{-2} per unit change in AOD over three hours in the early afternoon (Yu et al., 2016). These estimates depend on the model, cloud cover, and the thickness, extent and duration of the smoke. Our similarly wide range of 52 Wm^{-2} and 172 Wm^{-2} SWDS decreases for a single 16-day period using a single model with different configurations suggests possibly underestimated uncertainty in the radiative effects of smoke from other studies.

The connection between radiation absorption and scattering by smoke and cooler daytime surface temperatures was first inferred by Wexler (1950) from departures between the observed temperatures and those from pre-numerical weather forecasts, when smoke from a fire in northwestern Canada that arrived over the US was associated with ~5°C lower surface temperatures over a four-day period in Washington DC. Robock (1991) estimated temperature reductions ranging from 1.5°C to 7°C over parts of the U.S. following four different fire events with smoke plumes ranging in coverage from nearly all of Alaska or large swathes of temperate U.S., with durations of one to three days. Westphal and Toon (1991) estimated cooling of up to 5°C under smoke near Lake Winnipeg for half a day associated with the 1982 Eg Fire in British Columbia after scaling up their bottom-up aerosol emissions by a factor of three. Subsequent studies generally found that different fire events led to cooling of up to ~1°C to 6°C, including some that found weekly mean cooling of >1°C at either relatively local scales (Huang et al.,

692 2023; Mitchell et al., 2006; Stone et al., 2011) or regional scales of hundreds of thousands to
693 millions of km^2 (Jiang et al., 2012; Chang et al., 2021), seasonal cooling over western Russia of
694 0.4°C (Forkel et al., 2015) during the 2010 Russia fires, and up to a 4.4°C purported cooling over
695 southeastern Australia during a six-month period (Chang et al., 2021) after the 2019/2020
696 bushfire 'super outbreak' (Peterson et al., 2021).
697
698 Toll et al.'s (2015) estimates during the Russia 2010 of aerosol effects for six days over a ~1 000
699 000 km^2 area episode provides a good case for comparison. In two experiments with AOD
700 enhancements from the fires prescribed from observations and calculated prognostically from
701 emissions, the bias in 2m temperature was -0.43 ^{o}C and -1.1 ^{o}C, respectively, relative to a control
702 experiment with background aerosols only. Including the full hourly temperature over our
703 850,000 km^2 area over the six-day August 12-17 period, we estimated cooling between -1.7 ^{o}C
704 and -5.3 ^{o}C across ModelE members. This reinforces how strong the cooling was for the 2017
705 plume, but also that the range of estimates can be highly sensitive to the model configuration,
706 with the strongest cooling for the four experiments having variable injection heights and
707 MATRIX aerosols because of a stronger indirect effect.
708
709 Warming aloft from absorbing aerosols in the smoke layer was seen in previous studies for
710 single model time steps, for example in Grell et al.'s (2011) cross-sectional warming of up to 0.8
711 ^{o}C over Alaska for fires in 2004, Kochanski et al.'s (2019) warming of up to 0.5 ^{o}C over a single
712 location in California in 2015, and Walter et al.'s (2016) warming of up to 1^{o}C at Ft. Smith,
713 NWT in 2010. Our ModelE estimates over a 16-day period also showed this response (Figure
714 13), but with a magnitude ranging from 0.2 ^{o}C to 1.5 ^{o}C, peaking at different heights, and
715 strongest for the simulations with MATRIX aerosols and variable injection heights. Warming of
716 the smoke atmospheric layer and cooling at the surface can suppress the development of the
717 PBL, leading to a shallower PBL than in the absence of smoke. In studies where PBL height
718 reductions were examined, they ranged fairly widely, from a 200-400m reduction over western
719 Russia averaged over 21 days (Kong et al., 2015; Baro et al., 2017) and 400 m over the Trinity
720 River Valley in California over one day (Kochanski et al., 2019), through changes of >500 m for
721 one to a few days over western Russia and Salem, Oregon (Huang et al., 2023; Toll et al., 2015)
722 and of up to 1100 m for a single location in Montana over one hour (Jiang et al., 2012). In our

723 studies, the estimated reduction in PBL height averaged over 16 days was strongly configuration
724 dependent, ranging from 253m to 547m.
725
726 Model and observational studies have identified additional effects of wildfire smoke on
727 precipitation (Grell et al., 2011; Forkel et al., 2015; Kong et al., 2015; Semoutnikova et al., 2018;
728 Huang et al., 2023). We found only small effects on precipitation (not shown), likely because of
729 nudged winds which dampen local dynamical or precipitation responses, and possibly because of
730 ModelE's coarse-resolution convective parameterization, synoptic conditions not favorable to
731 precipitation in the first place, and, perhaps in this case, greater tropospheric stability caused by
732 the smoke-induced warming aloft, suggested to have occurred by Hodzic et al. (2007) for their
733 high resolution simulations of the fires over western Europe during the 2003 heat wave.
734 Similarly, though ModelE's vertical temperature structure was affected by the smoke, nudging
735 precluded any strong response in horizontal winds seen in free-running, higher-resolution
736 simulations (Kochanski et al., 2019; Mitchell et al., 2006; Pere et al., 2014), straightforward
737 diagnosis of surface pollution enhancements from PBL suppression (Pere et al., 2014; Kong et
738 al., 2015) or of positive feedbacks from smoke enhancing fire-conducive conditions such as
739 those near the west coast of the US during the 2020 fire season (Huang et al., 2023).

740 **5. Conclusions**

741 Across our small set of ModelE experiments, we captured the basic pattern of a re-circulating
742 smoke plume over northern Canada for August 12-27 observed in satellite retrievals of AOD and
743 CO. Over our large domain, the ModelE AOD bias relative to MODIS ranged from -0.15 to 0.19.
744 The CO bias over the mid troposphere ranged from 4 ppbv to 20 ppbv relative to MOPITT and
745 from 0 ppbv to 14 ppbv relative to AIRS. We found unanticipated interactions between the
746 choice of aerosol scheme, injection height approach and prescribed smoke emissions, namely
747 that a plausible configuration of the model resulted in anomalously high AOD through a
748 combination of high NO_x emissions in GFAS for boreal fuels, higher-altitude smoke injection
749 and the simplified OMA aerosol scheme. Moving beyond one-at-a-time sensitivity tests to a
750 structured experimental design was helpful in identifying this interaction. It was easier across our
751 experiments to identify these two outlying cases than to identify a 'best' model configuration or
752 group of model configurations, or to narrow the range of surface climate effects based on model

753 performance. The two outlying simulations did not have outlying climate effects. The more
754 apparent experiments with pronounced climate effects used the MATRIX microphysical aerosol
755 scheme and variable injection heights which led to stronger first indirect effects. Across all
756 experiments with different aerosol schemes, smoke emissions, injection heights and horizontal
757 winds, our estimates of smoke effects on PBL height ranged by a factor of two (-253 m to -547
758 m), and by a factor of three for short-wave downward solar radiation (-52 Wm^{-2} to -172 Wm^{-2})
759 and surface temperature (-1.5 ºC to -4.9 ºC), the latter spanning our independent estimate (-3.7
760 ºC) from the operational GFS forecast model.
761
762 Using more observational constraints, particularly of plume heights and in-situ measurements of
763 aerosol concentrations at the surface, will be helpful to more thoroughly compare model
764 configurations as we implement prognostic injection height parameterizations, incorporate new
765 emissions estimates such as those based on fire detections from VIIRS (Wiedinmyer et al.,
766 submitted; Ferrada et al., 2022) and geostationary instruments (Li et al., 2022; Nguyen et al.,
767 2023) which have previously improved modeled smoke (Hodzic et al., 2007), and ahead of
768 larger-scale and longer term estimates of climate effects and feedbacks with prognostic fire
769 models (Mezuman et al., 2020). For these cases, the number of structural options will increase,
770 and the experiments will also involve parametric changes. In this case, full factorial design
771 would become more challenging and a fractional factorial design more realistic.

772 **Acknowledgements**

773 This work was supported by NASA grant 80NSSC18K0166.

774 **Data availability**

775 All model simulations will be made available through the NASA Center for Climate Simulation
776 if the paper is published.

777 **References**

778 Baro, R., Lorente-Plazas, R., Montavez, J. P., and Jimenez-Guerrero, P.: Biomass burning
779 aerosol impact on surface winds during the 2010 Russian heat wave, Geophysical
780 Research Letters, 44, 1088-1094, 10.1002/2016gl071484, 2017.

781 Bauer, S. E. and Koch, D.: Impact of heterogeneous sulfate formation at mineral dust surfaces on
782 aerosol loads and radiative forcing in the Goddard Institute for Space Studies general
783 circulation model, Journal of Geophysical Research-Atmospheres, 110,
784 10.1029/2005jd005870, 2005.
785 Bauer, S. E. and Menon, S.: Aerosol direct, indirect, semidirect, and surface albedo effects from
786 sector contributions based on the IPCC AR5 emissions for preindustrial and present-day
787 conditions, Journal of Geophysical Research-Atmospheres, 117, 10.1029/2011jd016816,
788 2012.
789 Bauer, S. E., Ault, A. P., and Prather, K. A.: Evaluation of aerosol mixing state classes in the
790 GISS modelE-MATRIX climate model using single-particle mass spectrometry
791 measurements, Journal of Geophysical Research-Atmospheres, 118, 9834-9844,
792 10.1002/jgrd.50700, 2013.
793 Bauer, S. E., Menon, S., Koch, D., Bond, T. C., and Tsigaridis, K.: A global modeling study on
794 carbonaceous aerosol microphysical characteristics and radiative effects, Atmospheric
795 Chemistry and Physics, 10, 7439-7456, 10.5194/acp-10-7439-2010, 2010.
796 Bauer, S. E., Koch, D., Unger, N., Metzger, S. M., Shindell, D. T., and Streets, D. G.: Nitrate
797 aerosols today and in 2030: a global simulation including aerosols and tropospheric
798 ozone, Atmospheric Chemistry and Physics, 7, 5043-5059, 2007a.
799 Bauer, S. E., Mishchenko, M. I., Lacis, A. A., Zhang, S., Perlwitz, J., and Metzger, S. M.: Do
800 sulfate and nitrate coatings on mineral dust have important effects on radiative properties
801 and climate modeling?, Journal of Geophysical Research-Atmospheres, 112,
802 10.1029/2005jd006977, 2007b.
803 Bauer, S. E., Wright, D. L., Koch, D., Lewis, E. R., McGraw, R., Chang, L. S., Schwartz, S. E.,
804 and Ruedy, R.: MATRIX (Multiconfiguration Aerosol TRacker of mIXing state): an
805 aerosol microphysical module for global atmospheric models, Atmospheric Chemistry
806 and Physics, 8, 6003-6035, 2008.
807 Bauer, S. E., Tsigaridis, K., Faluvegi, G., Kelley, M., Lo, K. K., Miller, R. L., Nazarenko, L.,
808 Schmidt, G. A., and Wu, J. B.: Historical (1850-2014) Aerosol Evolution and Role on
809 Climate Forcing Using the GISS ModelE2.1 Contribution to CMIP6, Journal of
810 Advances in Modeling Earth Systems, 12, 10.1029/2019ms001978, 2020.

Carter, T. S., Heald, C. L., Jimenez, J. L., Campuzano-Jost, P., Kondo, Y., Moteki, N., Schwarz, J. P., Wiedinmyer, C., Darmenov, A. S., da Silva, A. M., and Kaiser, J. W.: How emissions uncertainty influences the distribution and radiative impacts of smoke from fires in North America, Atmospheric Chemistry and Physics, 20, 2073-2097, 10.5194/acp-20-2073-2020, 2020.

Chang, D. Y., Yoon, J., Lelieveld, J., Park, S. K., Yum, S. S., Kim, J., and Jeong, S.: Direct radiative forcing of biomass burning aerosols from the extensive Australian wildfires in 2019-2020, Environmental Research Letters, 16, 10.1088/1748-9326/abecfe, 2021.

Chubarova, N., Nezval, Y., Sviridenkov, I., Smirnov, A., and Slutsker, I.: Smoke aerosol and its radiative effects during extreme fire event over Central Russia in summer 2010, Atmospheric Measurement Techniques, 5, 557-568, 10.5194/amt-5-557-2012, 2012.

Das, S., Colarco, P. R., Oman, L. D., Taha, G., and Torres, O.: The long-term transport and radiative impacts of the 2017 British Columbia pyrocumulonimbus smoke aerosols in the stratosphere, Atmospheric Chemistry and Physics, 21, 12069-12090, 10.5194/acp-21-12069-2021, 2021.

Deeter, M. N., Edwards, D. P., Francis, G. L., Gille, J. C., Martinez-Alonso, S., Worden, H. M., and Sweeney, C.: A climate-scale satellite record for carbon monoxide: the MOPITT Version 7 product, Atmospheric Measurement Techniques, 10, 2533-2555, 10.5194/amt-10-2533-2017, 2017.

Eyring, V., Bony, S., Meehl, G. A., Senior, C. A., Stevens, B., Stouffer, R. J., and Taylor, K. E.: Overview of the Coupled Model Intercomparison Project Phase 6 (CMIP6) experimental design and organization, Geoscientific Model Development, 9, 1937-1958, 10.5194/gmd-9-1937-2016, 2016.

Ferrada, G. A., Zhou, M., Wang, J., Lyapustin, A., Wang, Y. J., Freitas, S. R., and Carmichael, G. R.: Introducing the VIIRS-based Fire Emission Inventory version 0 (VFEIv0), Geoscientific Model Development, 15, 8085-8109, 10.5194/gmd-15-8085-2022, 2022.

Field, R. D.: Evaluation of Global Fire Weather Database reanalysis and short-term forecast products, Natural Hazards and Earth System Sciences, 20, 1123-1147, 10.5194/nhess-20-1123-2020, 2020.

Forkel, R., Balzarini, A., Baro, R., Bianconi, R., Curci, G., Jimenez-Guerrero, P., Hirtl, M., Honzak, L., Lorenz, C., Im, U., Perez, J. L., Pirovano, G., San Jose, R., Tuccella, P.,

Werhahn, J., and Zabkar, R.: Analysis of the WRF-Chem contributions to AQMEII phase2 with respect to aerosol radiative feedbacks on meteorology and pollutant distributions, Atmospheric Environment, 115, 630-645, 10.1016/j.atmosenv.2014.10.056, 2015.

Fromm, M. D., Kablick, G. P., Peterson, D. A., Kahn, R. A., Flower, V. J. B., and Seftor, C. J.: Quantifying the Source Term and Uniqueness of the August 12, 2017 Pacific Northwest PyroCb Event, Journal of Geophysical Research-Atmospheres, 126, 10.1029/2021jd034928, 2021.

Fu, Y., Li, R., Huang, J., Bergeron, Y., Fu, Y., Wang, Y., and Gao, Z.: Satellite-Observed Impacts of Wildfires on Regional Atmosphere Composition and the Shortwave Radiative Forcing: A Multiple Case Study, Journal of Geophysical Research-Atmospheres, 123, 8326-8343, 10.1029/2017jd027927, 2018.

Gelaro, R., McCarty, W., Suarez, M. J., Todling, R., Molod, A., Takacs, L., Randles, C. A., Darmenov, A., Bosilovich, M. G., Reichle, R., Wargan, K., Coy, L., Cullather, R., Draper, C., Akella, S., Buchard, V., Conaty, A., da Silva, A. M., Gu, W., Kim, G. K., Koster, R., Lucchesi, R., Merkova, D., Nielsen, J. E., Partyka, G., Pawson, S., Putman, W., Rienecker, M., Schubert, S. D., Sienkiewicz, M., and Zhao, B.: The Modern-Era Retrospective Analysis for Research and Applications, Version 2 (MERRA-2), Journal of Climate, 30, 5419-5454, 10.1175/jcli-d-16-0758.1, 2017.

Gery, M. W., Whitten, G. Z., Killus, J. P., and Dodge, M. C.: A photochemical kinetics mechanism for urban and regional scale computer modeling, Journal of Geophysical Research-Atmospheres, 94, 12925-12956, 10.1029/JD094iD10p12925, 1989.

Gleeson, E., Toll, V., Nielsen, K. P., Rontu, L., and Masek, J.: Effects of aerosols on clear-sky solar radiation in the ALADIN-HIRLAM NWP system, Atmospheric Chemistry and Physics, 16, 5933-5948, 10.5194/acp-16-5933-2016, 2016.

Grell, G., Freitas, S. R., Stuefer, M., and Fast, J.: Inclusion of biomass burning in WRF-Chem: impact of wildfires on weather forecasts, Atmospheric Chemistry and Physics, 11, 5289-5303, 10.5194/acp-11-5289-2011, 2011.

Guenther, A. B., Zimmerman, P. R., Harley, P. C., Monson, R. K., and Fall, R.: Isoprene and monoterpene emission rate variability - model evaluations and sensitivity analyses,

872 Journal of Geophysical Research-Atmospheres, 98, 12609-12617, 10.1029/93jd00527,
873 1993.
874 Hodzic, A., Madronich, S., Bohn, B., Massie, S., Menut, L., and Wiedinmyer, C.: Wildfire
875 particulate matter in Europe during summer 2003: meso-scale modeling of smoke
876 emissions, transport and radiative effects, Atmospheric Chemistry and Physics, 7, 4043-
877 4064, 10.5194/acp-7-4043-2007, 2007.
878 Hoesly, R. M., Smith, S. J., Feng, L. Y., Klimont, Z., Janssens-Maenhout, G., Pitkanen, T.,
879 Seibert, J. J., Vu, L., Andres, R. J., Bolt, R. M., Bond, T. C., Dawidowski, L., Kholod, N.,
880 Kurokawa, J., Li, M., Liu, L., Lu, Z. F., Moura, M. C. P., O'Rourke, P. R., and Zhang, Q.:
881 Historical (1750-2014) anthropogenic emissions of reactive gases and aerosols from the
882 Community Emissions Data System (CEDS), Geoscientific Model Development, 11,
883 369-408, 10.5194/gmd-11-369-2018, 2018.
884 Huang, X., Ding, K., Liu, J., Wang, Z., Tang, R., Xue, L., Wang, H., Zhang, Q., Tan, Z.-M., Fu,
885 C., Davis, S. J., Andreae, M. O., and Ding, A.: Smoke-weather interaction affects
886 extreme wildfires in diverse coastal regions, Science, 379, 457-461,
887 10.1126/science.add9843, 2023.
888 Hubanks, P., Platnick, S., King, M., and Ridgway, B.: MODIS Algorithm Theoretical Basis
889 Document No. ATBD-MOD-30 for Level-3 Global Gridded Atmosphere Products
890 (08_D3, 08_E3, 08_M3) and Users Guide (Collection 6.0 & 6.1, Version 4.4, 20 Feb
891 2019), NASA Goddard Space Flight Center, Greenbelt, MD, 2019.
892 Huijnen, V., Flemming, J., Kaiser, J. W., Inness, A., Leitao, J., Heil, A., Eskes, H. J., Schultz, M.
893 G., Benedetti, A., Hadji-Lazaro, J., Dufour, G., and Eremenko, M.: Hindcast experiments
894 of tropospheric composition during the summer 2010 fires over western Russia,
895 Atmospheric Chemistry and Physics, 12, 4341-4364, 10.5194/acp-12-4341-2012, 2012.
896 Jiang, X. Y., Wiedinmyer, C., and Carlton, A. G.: Aerosols from Fires: An Examination of the
897 Effects on Ozone Photochemistry in the Western United States, Environmental Science &
898 Technology, 46, 11878-11886, 10.1021/es301541k, 2012.
899 Jones, T., Ahmadov, R., James, E., Pereira, G., Freitas, S., and Grell, G.: Prototype of a Warn-
900 on-Forecast System for Smoke (WoFS-Smoke), Weather and Forecasting, 37, 1191-
901 1209, 10.1175/waf-d-21-0143.1, 2022.

902 Juliano, T. W., Jimenez, P. A., Kosovic, B., Eidhammer, T., Thompson, G., Berg, L. K., Fast, J.,
903 Motley, A., and Polidori, A.: Smoke from 2020 United States wildfires responsible for
904 substantial solar energy forecast errors, Environmental Research Letters, 17,
905 10.1088/1748-9326/ac5143, 2022.
906 Kaiser, J. W., Heil, A., Andreae, M. O., Benedetti, A., Chubarova, N., Jones, L., Morcrette, J. J.,
907 Razinger, M., Schultz, M. G., Suttie, M., and van der Werf, G. R.: Biomass burning
908 emissions estimated with a global fire assimilation system based on observed fire
909 radiative power, Biogeosciences, 9, 527-554, 10.5194/bg-9-527-2012, 2012.
910 Kalnay, E., Kanamitsu, M., Kistler, R., Collins, W., Deaven, D., Gandin, L., Iredell, M., Saha,
911 S., White, G., Woollen, J., Zhu, Y., Chelliah, M., Ebisuzaki, W., Higgins, W., Janowiak,
912 J., Mo, K. C., Ropelewski, C., Wang, J., Leetmaa, A., Reynolds, R., Jenne, R., and
913 Joseph, D.: The NCEP/NCAR 40-year reanalysis project, Bulletin of the American
914 Meteorological Society, 77, 437-471, 10.1175/1520-
915 0477(1996)077<0437:tnyrp>2.0.co;2, 1996.
916 Kelley, M., Schmidt, G. A., Nazarenko, L. S., Bauer, S. E., Ruedy, R., Russell, G. L., Ackerman,
917 A. S., Aleinov, I., Bauer, M., Bleck, R., Canuto, V., Cesana, G., Cheng, Y., Clune, T. L.,
918 Cook, B., Cruz, C. A., Del Genio, A. D., Elsaesser, G. S., Faluvegi, G., Kiang, N. Y.,
919 Kim, D., Lacis, A. A., Leboissetier, A., LeGrande, A. N., Lo, K. K., Marshall, J.,
920 Matthews, E. E., McDermid, S., Mezuman, K., Miller, R. L., Murray, L. T., Oinas, V.,
921 Orbe, C., Garcia-Pando, C. P., Perlwitz, J. P., Puma, M. J., Rind, D., Romanou, A.,
922 Shindell, D. T., Sun, S., Tausnev, N., Tsigaridis, K., Tselioudis, G., Weng, E. S., Wu, J.
923 B., and Yao, M. S.: GISS-E2.1: Configurations and Climatology, Journal of Advances in
924 Modeling Earth Systems, 12, 10.1029/2019ms002025, 2020.
925 Koch, D., Schmidt, G. A., and Field, C. V.: Sulfur, sea salt, and radionuclide aerosols in GISS
926 ModelE, Journal of Geophysical Research-Atmospheres, 111, 10.1029/2004jd005550,
927 2006.
928 Kochanski, A. K., Mallia, D. V., Fearon, M. G., Mandel, J., Souri, A. H., and Brown, T.:
929 Modeling Wildfire Smoke Feedback Mechanisms Using a Coupled Fire-Atmosphere
930 Model With a Radiatively Active Aerosol Scheme, Journal of Geophysical Research-
931 Atmospheres, 124, 9099-9116, 10.1029/2019jd030558, 2019.

Kong, X., Forkel, R., Sokhi, R. S., Suppan, P., Baklanov, A., Gauss, M., Brunner, D., Baro, R., Balzarini, A., Chemel, C., Curci, G., Jimenez-Guerrero, P., Hirtl, M., Honzak, L., Im, U., Perez, J. L., Pirovano, G., San Jose, R., Schlunzen, K. H., Tsegas, G., Tuccella, P., Werhahn, J., Zabkar, R., and Galmarini, S.: Analysis of meteorology-chemistry interactions during air pollution episodes using online coupled models within AQMEII phase-2, Atmospheric Environment, 115, 527-540, 10.1016/j.atmosenv.2014.09.020, 2015.

Konovalov, I. B., Golovushkin, N. A., Beekmann, M., and Andreae, M. O.: Insights into the aging of biomass burning aerosol from satellite observations and 3D atmospheric modeling: Evolution of the aerosol optical properties in Siberian wildfire plumes, Atmos. Chem. Phys. Discuss., 2020, 1-54, 10.5194/acp-2020-591, 2020.

Kopacz, M., Jacob, D. J., Fisher, J. A., Logan, J. A., Zhang, L., Megretskaia, I. A., Yantosca, R. M., Singh, K., Henze, D. K., Burrows, J. P., Buchwitz, M., Khlystova, I., McMillan, W. W., Gille, J. C., Edwards, D. P., Eldering, A., Thouret, V., and Nedelec, P.: Global estimates of CO sources with high resolution by adjoint inversion of multiple satellite datasets (MOPITT, AIRS, SCIAMACHY, TES), Atmospheric Chemistry and Physics, 10, 855-876, 2010.

Lestrelin, H., Legras, B., Podglajen, A., and Salihoglu, M.: Smoke-charged vortices in the stratosphere generated by wildfires and their behaviour in both hemispheres: comparing Australia 2020 to Canada 2017, Atmospheric Chemistry and Physics, 21, 7113-7134, 10.5194/acp-21-7113-2021, 2021.

Li, F. J., Zhang, X. Y., Kondragunta, S., Lu, X. M., Csiszar, I., and Schmidt, C. C.: Hourly biomass burning emissions product from blended geostationary and polar-orbiting satellites for air quality forecasting applications, Remote Sensing of Environment, 281, 10.1016/j.rse.2022.113237, 2022.

Liu, Y. W., Zhang, K., Qian, Y., Wang, Y. H., Zou, Y. F., Song, Y. J., Wan, H., Liu, X. H., and Yang, X. Q.: Investigation of short-term effective radiative forcing of fire aerosols over North America using nudged hindcast ensembles, Atmospheric Chemistry and Physics, 18, 31-47, 10.5194/acp-18-31-2018, 2018.

961 Lu, Z. and Sokolik, I. N.: The effect of smoke emission amount on changes in cloud properties
962 and precipitation: A case study of Canadian boreal wildfires of 2007, Journal of
963 Geophysical Research-Atmospheres, 118, 11777-11793, 10.1002/2013jd019860, 2013.
964 Mallet, M., Solmon, F., Roblou, L., Peers, F., Turquety, S., Waquet, F., Jethva, H., and Torres,
965 O.: Simulation of Optical Properties and Direct and Indirect Radiative Effects of Smoke
966 Aerosols Over Marine Stratocumulus Clouds During Summer 2008 in California With
967 the Regional Climate Model RegCM, Journal of Geophysical Research-Atmospheres,
968 122, 10288-10313, 10.1002/2017jd026905, 2017.
969 McKendry, I. G., Christen, A., Lee, S. C., Ferrara, M., Strawbridge, K. B., O'Neill, N., and
970 Black, A.: Impacts of an intense wildfire smoke episode on surface radiation, energy and
971 carbon fluxes in southwestern British Columbia, Canada, Atmospheric Chemistry and
972 Physics, 19, 835-846, 10.5194/acp-19-835-2019, 2019.
973 McMillan, W. W., Evans, K. D., Barnet, C. D., Maddy, E. S., Sachse, G. W., and Diskin, G. S.:
974 Validating the AIRS Version 5 CO Retrieval With DACOM In Situ Measurements
975 During INTEX-A and -B, Ieee Transactions on Geoscience and Remote Sensing, 49,
976 2802-2813, 10.1109/tgrs.2011.2106505, 2011.
977 Menon, S. and Rotstayn, L.: The radiative influence of aerosol effects on liquid-phase cumulus
978 and stratiform clouds based on sensitivity studies with two climate models, Climate
979 Dynamics, 27, 345-356, 10.1007/s00382-006-0139-3, 2006.
980 Metzger, S., Dentener, F., Pandis, S., and Lelieveld, J.: Gas/aerosol partitioning: 1. A
981 computationally efficient model, Journal of Geophysical Research-Atmospheres, 107,
982 10.1029/2001jd001102, 2002.
983 Mezuman, K., Tsigaridis, K., Faluvegi, G., and Bauer, S. E.: The interactive global fire module
984 pyrE (v1.0), Geoscientific Model Development, 13, 3091-3118, 10.5194/gmd-13-3091-
985 2020, 2020.
986 Miller, R. L., Cakmur, R. V., Perlwitz, J., Geogdzhayev, I. V., Ginoux, P., Koch, D., Kohfeld, K.
987 E., Prigent, C., Ruedy, R., Schmidt, G. A., and Tegen, I.: Mineral dust aerosols in the
988 NASA goddard institute for Space Sciences ModelE atmospheric general circulation
989 model, Journal of Geophysical Research-Atmospheres, 111, 10.1029/2005jd005796,
990 2006.

991 Miller, R. L., Schmidt, G. A., Nazarenko, L. S., Tausnev, N., Bauer, S. E., DelGenio, A. D.,
992 Kelley, M., Lo, K. K., Ruedy, R., Shindell, D. T., Aleinov, I., Bauer, M., Bleck, R.,
993 Canuto, V., Chen, Y. H., Cheng, Y., Clune, T. L., Faluvegi, G., Hansen, J. E., Healy, R.
994 J., Kiang, N. Y., Koch, D., Lacis, A. A., LeGrande, A. N., Lerner, J., Menon, S., Oinas,
995 V., Garcia-Pando, C. P., Perlwitz, J. P., Puma, M. J., Rind, D., Romanou, A., Russell, G.
996 L., Sato, M., Sun, S., Tsigaridis, K., Unger, N., Voulgarakis, A., Yao, M. S., and Zhang,
997 J. L.: CMIP5 historical simulations (1850-2012) with GISS ModelE2, Journal of
998 Advances in Modeling Earth Systems, 6, 441-477, 10.1002/2013ms000266, 2014.
999 Mitchell, R. M., O'Brien, D. M., and Campbell, S. K.: Characteristics and radiative impact of the
1000 aerosol generated by the Canberra firestorm of January 2003, Journal of Geophysical
1001 Research-Atmospheres, 111, 10.1029/2005jd006304, 2006.
1002 Montgomery, D. C., 8 (Ed.): Design and Analysis of Experiments, John Wiley and Sons, Inc.,
1003 Hoboken, NJ, 752 pp.2013.
1004 Nguyen, H. M., He, J. P., and Wooster, M. J.: Biomass burning CO, PM and fuel consumption
1005 per unit burned area estimates derived across Africa using geostationary SEVIRI fire
1006 radiative power and Sentinel-5P CO data, Atmospheric Chemistry and Physics, 23, 2089-
1007 2118, 10.5194/acp-23-2089-2023, 2023.
1008 Palacios-Peña , L., Stier, P., Lorente-Plazas, R., and Jimenez-Guerrero, P.: Quantifying the
1009 sensitivity of aerosol optical properties to the parameterizations of physico-chemical
1010 processes during the 2010 Russian wildfires and heatwave, Atmospheric Chemistry and
1011 Physics, 20, 9679-9700, 10.5194/acp-20-9679-2020, 2020.
1012 Palacios-Peña , L., Baro, R., Baklanov, A., Balzarini, A., Brunner, D., Forkel, R., Hirtl, M.,
1013 Honzak, L., Lopez-Romero, J. M., Montavez, J. P., Perez, J. L., Pirovano, G., Jose, R. S.,
1014 Schroder, W., Werhahn, J., Wolke, R., Zabkar, R., and Jimenez-Guerrero, P.: An
1015 assessment of aerosol optical properties from remote-sensing observations and regional
1016 chemistry-climate coupled models over Europe, Atmospheric Chemistry and Physics, 18,
1017 5021-5043, 10.5194/acp-18-5021-2018, 2018.
1018 Pan, X., Ichoku, C., Chin, M., Bian, H., Darmenov, A., Colarco, P., Ellison, L., Kucsera, T., da
1019 Silva, A., Wang, J., Oda, T., and Cui, G.: Six global biomass burning emission datasets:
1020 intercomparison and application in one global aerosol model, Atmos. Chem. Phys., 20,
1021 969-994, 10.5194/acp-20-969-2020, 2020.

Pere, J. C., Bessagnet, B., Pont, V., Mallet, M., and Minvielle, F.: Influence of the aerosol solar extinction on photochemistry during the 2010 Russian wildfires episode, Atmospheric Chemistry and Physics, 15, 10983-10998, 10.5194/acp-15-10983-2015, 2015.

Pere, J. C., Bessagnet, B., Mallet, M., Waquet, F., Chiapello, I., Minvielle, F., Pont, V., and Menut, L.: Direct radiative effect of the Russian wildfires and its impact on air temperature and atmospheric dynamics during August 2010, Atmospheric Chemistry and Physics, 14, 1999-2013, 10.5194/acp-14-1999-2014, 2014.

Peterson, D. A., Campbell, J. R., Hyer, E. J., Fromm, M. D., Kablick, G. P., Cossuth, J. H., and DeLand, M. T.: Wildfire-driven thunderstorms cause a volcano-like stratospheric injection of smoke, npj Climate and Atmospheric Science, 1, 10.1038/s41612-018-0039-3, 2018.

Peterson, D. A., Fromm, M. D., McRae, R. H. D., Campbell, J. R., Hyer, E. J., Taha, G., Camacho, C. P., Kablick, G. P., Schmidt, C. C., and DeLand, M. T.: Australia's Black Summer pyrocumulonimbus super outbreak reveals potential for increasingly extreme stratospheric smoke events, Npj Climate and Atmospheric Science, 4, 10.1038/s41612-021-00192-9, 2021.

Rayner, N. A., Parker, D. E., Horton, E. B., Folland, C. K., Alexander, L. V., Rowell, D. P., Kent, E. C., and Kaplan, A.: Global analyses of sea surface temperature, sea ice, and night marine air temperature since the late nineteenth century, Journal of Geophysical Research-Atmospheres, 108, 10.1029/2002jd002670, 2003.

Remy, S., Veira, A., Paugam, R., Sofiev, M., Kaiser, J. W., Marenco, F., Burton, S. P., Benedetti, A., Engelen, R. J., Ferrare, R., and Hair, J. W.: Two global data sets of daily fire emission injection heights since 2003, Atmospheric Chemistry and Physics, 17, 2921-2942, 10.5194/acp-17-2921-2017, 2017.

Robock, A.: Enhancement of Surface Cooling Due to Forest Fire Smoke, Science, 242, 911-913, 10.1126/science.242.4880.911, 1988.

Robock, A.: Surface cooling due to forest-fire smoke, Journal of Geophysical Research-Atmospheres, 96, 20869-20878, 10.1029/91jd02043, 1991.

Santos, D., Costa, M. J., and Silva, A. M.: Direct SW aerosol radiative forcing over portugal, Atmospheric Chemistry and Physics, 8, 5771-5786, 10.5194/acp-8-5771-2008, 2008.

Sayer, A. M., Munchak, L. A., Hsu, N. C., Levy, R. C., Bettenhausen, C., and Jeong, M. J.: MODIS Collection 6 aerosol products: Comparison between Aqua's e-Deep Blue, Dark Target, and "merged" data sets, and usage recommendations, Journal of Geophysical Research-Atmospheres, 119, 13965-13989, 10.1002/2014jd022453, 2014.

Semoutnikova, E. G., Gorchakov, G. I., Sitnov, S. A., Kopeikin, V. M., Karpov, A. V., Gorchakova, I. A., Ponomareva, T. Y., Isakov, A. A., Gushchin, R. A., Datsenko, O. I., Kurbatov, G. A., and Kuznetsov, G. A.: Siberian Smoke Haze over European Territory of Russia in July 2016: Atmospheric Pollution and Radiative Effects, Atmospheric and Oceanic Optics, 31, 171-180, 10.1134/s1024856018020124, 2018.

Sexton, D. M. H., Grubb, H., Shine, K. P., and Folland, C. K.: Design and analysis of climate model experiments for the efficient estimation of anthropogenic signals, Journal of Climate, 16, 1320-1336, 10.1175/1520-0442-16.9.1320, 2003.

Smith, A., Lott, N., and Vose, R.: The Integrated Surface Database Recent Developments and Partnerships, Bulletin of the American Meteorological Society, 92, 704-708, 10.1175/2011bams3015.1, 2011.

Smith, N. and Barnet, C. D.: Uncertainty Characterization and Propagation in the Community Long-Term Infrared Microwave Combined Atmospheric Product System (CLIMCAPS), Remote Sensing, 11, 10.3390/rs11101227, 2019.

Smith, N. and Barnet, C. D.: CLIMCAPS observing capability for temperature, moisture, and trace gases from AIRS/AMSU and CrIS/ATMS, Atmospheric Measurement Techniques, 13, 4437-4459, 10.5194/amt-13-4437-2020, 2020.

Stocks, B. J., Lawson, B. D., Alexander, M. E., Vanwagner, C. E., McAlpine, R. S., Lynham, T. J., and Dube, D. E.: The Canadian Forest Fire Danger Rating System - An Overview, Forestry Chronicle, 65, 450-457, 1989.

Stone, R. S., Augustine, J. A., Dutton, E. G., O'Neill, N. T., and Saha, A.: Empirical determinations of the longwave and shortwave radiative forcing efficiencies of wildfire smoke, Journal of Geophysical Research-Atmospheres, 116, 10.1029/2010jd015471, 2011.

Tang, I. N. and Munkelwitz, H. R.: Aerosol phase-transformation and growth in the atmosphere, Journal of Applied Meteorology, 33, 791-796, 10.1175/1520-0450(1994)033<0791:aptagi>2.0.co;2, 1994.

Toll, V., Reis, K., Ots, R., Kaasik, M., Maennik, A., Prank, M., and Sofiev, M.: SILAM and MACC reanalysis aerosol data used for simulating the aerosol direct radiative effect with the NWP model HARMONIE for summer 2010 wildfire case in Russia, Atmospheric Environment, 121, 75-85, 10.1016/j.atmosenv.2015.06.007, 2015.

Torres, O., Bhartia, P. K., Taha, G., Jethva, H., Das, S., Colarco, P., Krotkov, N., Omar, A., and Ahn, C.: Stratospheric Injection of Massive Smoke Plume From Canadian Boreal Fires in 2017 as Seen by DSCOVR-EPIC, CALIOP, and OMPS-LP Observations, Journal of Geophysical Research-Atmospheres, 125, 10.1029/2020jd032579, 2020.

Tsigaridis, K. and Kanakidou, M.: Secondary organic aerosol importance in the future atmosphere, Atmospheric Environment, 41, 4682-4692, 10.1016/j.atmosenv.2007.03.045, 2007.

Tsigaridis, K. and Kanakidou, M.: The Present and Future of Secondary Organic Aerosol Direct Forcing on Climate, Current Climate Change Reports, 4, 84-98, 10.1007/s40641-018-0092-3, 2018.

Tsigaridis, K., Koch, D., and Menon, S.: Uncertainties and importance of sea spray composition on aerosol direct and indirect effects, Journal of Geophysical Research-Atmospheres, 118, 220-235, 10.1029/2012jd018165, 2013.

Twomey, S.: Influence of pollution on shortwave albedo of clouds, Journal of the Atmospheric Sciences, 34, 1149-1152, 10.1175/1520-0469(1977)034<1149:tiopot>2.0.co;2, 1977.

van der Werf, G. R., Randerson, J. T., Giglio, L., van Leeuwen, T. T., Chen, Y., Rogers, B. M., Mu, M. Q., van Marle, M. J. E., Morton, D. C., Collatz, G. J., Yokelson, R. J., and Kasibhatla, P. S.: Global fire emissions estimates during 1997-2016, Earth System Science Data, 9, 697-720, 10.5194/essd-9-697-2017, 2017.

Vehkamaki, H., Kulmala, M., Napari, I., Lehtinen, K. E. J., Timmreck, C., Noppel, M., and Laaksonen, A.: An improved parameterization for sulfuric acid-water nucleation rates for tropospheric and stratospheric conditions, Journal of Geophysical Research-Atmospheres, 107, 10.1029/2002jd002184, 2002.

Walter, C., Freitas, S. R., Kottmeier, C., Kraut, I., Rieger, D., Vogel, H., and Vogel, B.: The importance of plume rise on the concentrations and atmospheric impacts of biomass burning aerosol, Atmospheric Chemistry and Physics, 16, 9201-9219, 10.5194/acp-16-9201-2016, 2016.

Warner, J., Carminati, F., Wei, Z., Lahoz, W., and Attie, J. L.: Tropospheric carbon monoxide variability from AIRS under clear and cloudy conditions, Atmospheric Chemistry and Physics, 13, 12469-12479, 10.5194/acp-13-12469-2013, 2013.

Westphal, D. L. and Toon, O. B.: Simulations of microphysical, radiative, and dynamic processes in a continental-scale forest-fire smoke plume, Journal of Geophysical Research-Atmospheres, 96, 22379-22400, 10.1029/91jd01956, 1991.

Wexler, H.: The Great Smoke Pall - September 24-30, 1950, Weatherwise, 3, 129-142, 1950.

Wiedinmyer, C., Kimura, Y., McDonald-Buller, E. C., Emmons, L. K., Buchholz, R. R., Tang, W., Seto, K., Joseph, M. B., Barsanti, K. C., Carlton, A. G., and Yokelson, R.: The Fire Inventory from NCAR version 2.5: an updated global fire emissions model for climate and chemistry applications, EGUSphere, 2023, 10.5194/egusphere-2023-124, submitted.

Witte, J. C., Douglass, A. R., da Silva, A., Torres, O., Levy, R., and Duncan, B. N.: NASA A-Train and Terra observations of the 2010 Russian wildfires, Atmospheric Chemistry and Physics, 11, 9287-9301, 10.5194/acp-11-9287-2011, 2011.

Wizenberg, T., Strong, K., Jones, D. B. A., Lutsch, E., Mahieu, E., Franco, B., and Clarisse, L.: Exceptional Wildfire Enhancements of PAN, C2H4, CH3OH, and HCOOH Over the Canadian High Arctic During August 2017, Journal of Geophysical Research - Atmospheres, doi: 10.1029/2022JD038052, in press.

Yu, P. F., Toon, O. B., Bardeen, C. G., Zhu, Y. Q., Rosenlof, K. H., Portmann, R. W., Thornberry, T. D., Gao, R. S., Davis, S. M., Wolf, E. T., de Gouw, J., Peterson, D. A., Fromm, M. D., and Robock, A.: Black carbon lofts wildfire smoke high into the stratosphere to form a persistent plume, Science, 365, 587-590, 10.1126/science.aax1748, 2019.

Yu, P. F., Toon, O. B., Bardeen, C. G., Bucholtz, A., Rosenlof, K. H., Saide, P. E., Da Silva, A., Ziemba, L. D., Thornhill, K. L., Jimenez, J. L., Campuzano-Jost, P., Schwarz, J. P., Perring, A. E., Froyd, K. D., Wagner, N. L., Mills, M. J., and Reid, J. S.: Surface dimming by the 2013 Rim Fire simulated by a sectional aerosol model, Journal of Geophysical Research-Atmospheres, 121, 7079-7087, 10.1002/2015jd024702, 2016.

Tables

Table 1. List of ModelE simulations and the aerosol module, emissions from biomass burning, injection height scheme, and horizontal winds used for nudging for each. The four-letter AEIW code at the end of each experiment indicates the factor levels (Aerosols: (O)MA or (M)ATRIX; Emissions: GFA(S) or GFE(D); Injection height: (P)BL or (V)ARIABLE; Winds: (M)ERRA2 or (N)CEP).

Simulation name (NN_AEIW)	Aerosols (A)	Emissions from biomass burning (E)	Injection height (I)	Nudging winds (W)
01_OSPM	OMA	GFAS	PBL	MERRA2
02_MSPM	MATRIX	GFAS	PBL	MERRA2
03_ODPM	OMA	GFED	PBL	MERRA2
04_MDPM	MATRIX	GFED	PBL	MERRA2
05_OSVM	OMA	GFAS	VARIABLE	MERRA2
06_MSVM	MATRIX	GFAS	VARIABLE	MERRA2
07_ODVM	OMA	GFED	VARIABLE	MERRA2
08_MDVM	MATRIX	GFED	VARIABLE	MERRA2
09_OSPN	OMA	GFAS	PBL	NCEP
10_MSPN	MATRIX	GFAS	PBL	NCEP
11_ODPN	OMA	GFED	PBL	NCEP
12_MDPN	MATRIX	GFED	PBL	NCEP
13_OSVN	OMA	GFAS	VARIABLE	NCEP
14_MSVN	MATRIX	GFAS	VARIABLE	NCEP
15_ODVN	OMA	GFED	VARIABLE	NCEP
16_MDVN	MATRIX	GFED	VARIABLE	NCEP

Table 2. Mean AOD and CO for the 16 ModelE simulations in Table 1 and bias, root-mean square error (RMSE) and pattern correlation (corr) relative to MODIS AOD, MOPITT CO, and AIRS CO. Statistics are during August 12-27, 2017 over the large analysis domain (50°N to 85°N, 140°W to 90°W).

	Relative to MODIS AOD				Relative to MOPITT CO				Relative to AIRS CO			
NAME	ModelE Mean	Bias	RMSE	corr	ModelE Mean (ppbv)	Bias	RMSE	corr	ModelE Mean (ppbv)	Bias	RMSE	corr
01_OSPM	0.43	0.00	0.32	0.75	127.6	5.8	18.1	0.76	118.2	1.9	10.8	0.87
02_MSPM	0.34	-0.09	0.34	0.71	127.6	6.8	17.3	0.78	120.3	4.1	11.1	0.88
03_ODPM	0.32	-0.11	0.32	0.71	127.5	5.6	20.5	0.69	117.8	1.6	11.0	0.85
04_MDPM	0.31	-0.12	0.34	0.69	127.4	6.3	18.9	0.71	119.7	3.4	11.2	0.85
05_OSVM	0.60	0.17	0.48	0.69	141.0	20.1	40.5	0.66	127.7	11.5	15.6	0.92
06_MSVM	0.43	0.00	0.37	0.70	136.2	15.9	29.6	0.67	130.4	14.1	19.0	0.89
07_ODVM	0.39	-0.04	0.33	0.68	138.9	18.0	38.2	0.67	124.4	8.1	12.0	0.91
08_MDVM	0.37	-0.06	0.35	0.69	138.1	17.9	31.2	0.68	130.5	14.2	19.3	0.89
09_OSPN	0.40	-0.03	0.34	0.67	125.4	4.0	19.4	0.70	117.7	1.4	13.9	0.80
10_MSPN	0.31	-0.12	0.38	0.58	127.4	6.4	19.2	0.71	120.9	4.6	13.4	0.85
11_ODPN	0.28	-0.15	0.36	0.65	123.5	2.2	20.1	0.65	115.8	-0.4	14.0	0.78
12_MDPN	0.28	-0.15	0.38	0.57	125.9	4.9	19.3	0.68	119.1	2.8	12.7	0.85
13_OSVN	0.62	0.19	0.52	0.67	137.9	16.4	28.0	0.76	125.2	9.0	13.5	0.91
14_MSVN	0.42	-0.01	0.39	0.64	134.4	13.7	26.4	0.68	129.4	13.2	18.4	0.87
15_ODVN	0.37	-0.06	0.34	0.63	133.5	12.2	24.6	0.73	121.1	4.8	9.9	0.90
16_MDVN	0.37	-0.06	0.38	0.61	137.2	16.2	31.6	0.65	128.9	12.7	17.7	0.89

Table 3. Regression estimates for ModelE bias, root-mean squared error (RMSE) and pattern correlation during August 12-27, 2017 over the large analysis domain (50°N to 85°N, 140°W to 90°W) compared to MODIS AOD for aerosols (A), emissions (E), injection height (I) and nudging winds (W) and second-order interactions between them. Estimates where p < .05 have been bolded for clarity. The main or interaction effects are the twice the b_i coefficient values.

	Bias		RMSE		Pattern correlation	
	Estimate	p	Estimate	p	Estimate	p
b_0	-0.039	0.001	0.373	0.000	0.665	0.000
b_1 (A)	**-0.036**	**0.002**	-0.005	0.589	**-0.016**	**0.002**
b_2 (E)	**-0.054**	**0.000**	-0.021	0.062	**-0.009**	**0.015**
b_3 (I)	**0.056**	**0.000**	**0.023**	**0.047**	-0.001	0.728
b_4 (W)	-0.008	0.212	0.015	0.153	**-0.037**	**0.000**
b_5 (AE)	**0.032**	**0.003**	0.019	0.091	0.002	0.381
b_6 (AI)	-0.012	0.087	-0.018	0.106	**0.012**	**0.006**
b_7 (AW)	0.000	0.972	0.002	0.843	-0.009	0.014
b_8 (EI)	**-0.018**	**0.028**	**-0.023**	**0.047**	0.000	0.891
b_9 (EW)	-0.002	0.699	0.000	0.974	-0.002	0.522
b_{10} (IW)	0.007	0.281	-0.003	0.780	**0.011**	**0.007**

Table 4. Same as Table 3, but for MOPITT CO.

	Bias		RMSE		corr	
	Estimate	p	Estimate	p	Estimate	p
b_0	10.8	0.000	25.2	0.000	0.699	0.000
b_1 (A)	0.2	0.503	-1.0	0.257	-0.002	0.768
b_2 (E)	-0.4	0.321	0.4	0.642	**-0.017**	**0.046**
b_3 (I)	**5.5**	**0.000**	**6.1**	**0.001**	-0.011	0.128
b_4 (W)	**-1.3**	**0.013**	-1.6	0.090	-0.005	0.493
b_5 (AE)	0.7	0.100	0.7	0.409	0.001	0.828
b_6 (AI)	-0.6	0.131	-0.6	0.492	-0.014	0.074
b_7 (AW)	0.6	0.150	1.5	0.101	-0.011	0.128
b_8 (EI)	0.1	0.712	-0.2	0.781	0.010	0.165
b_9 (EW)	-0.3	0.460	0.0	0.952	-0.001	0.879
b_{10} (IW)	-0.4	0.277	-2.0	0.047	**0.021**	**0.020**

Table 5. Same as Table 3, but for AIRS CO.

	Bias		RMSE		corr	
	Estimate	p	Estimate	p	Estimate	p
b_0	6.7	0.000	14.0	0.000	0.869	0.000
b_1 (A)	**2.0**	**0.000**	**1.4**	**0.003**	0.002	0.481
b_2 (E)	**-0.8**	**0.013**	-0.5	0.105	-0.003	0.322
b_3 (I)	**4.3**	**0.000**	**1.7**	**0.001**	**0.028**	**0.000**
b_4 (W)	**-0.7**	**0.023**	0.2	0.422	**-0.013**	**0.008**
b_5 (AE)	0.4	0.094	0.4	0.200	0.004	0.301
b_6 (AI)	**0.7**	**0.026**	**1.6**	**0.002**	**-0.014**	**0.006**
b_7 (AW)	0.4	0.145	0.0	0.921	0.008	0.054
b_8 (EI)	-0.2	0.371	-0.4	0.134	0.004	0.210
b_9 (EW)	-0.3	0.277	-0.1	0.644	0.003	0.363
b_{10} (IW)	-0.4	0.141	**-1.0**	**0.010**	**0.009**	**0.032**

Table 6. Average surface climate effects of smoke over the small region during August 12-27, 2017 for the 16 ModelE simulations in Table 1. Each average is the difference between the fire and its corresponding no-fire experiment. Experiments with a * were in poor agreement with MODIS AOD.

NAME	Change in shortwave downward radiation at surface (Wm^{-2})	Change in PBL Height (m)	Change in surface temperature (^oC)
01_OSPM	-82	-314	-2.2
02_MSPM	-134	-453	-3.4
03_ODPM	-63	-253	-1.7
04_MDPM	-122	-417	-3.0
05_OSVM (*)	-102	-415	-3.1
06_MSVM	-161	-504	-4.7
07_ODVM	-87	-333	-2.3
08_MDVM	-140	-507	-4.1
09_OSPN	-78	-327	-2.0
10_MSPN	-127	-453	-3.2
11_ODPN	-53	-261	-1.4
12_MDPN	-114	-436	-2.8
13_OSVN (*)	-117	-466	-3.4
14_MSVN	-172	-545	-4.9
15_ODVN	-87	-363	-2.3
16_MDVN	-156	-547	-4.4

Table 7. Regression estimates for ModelE surface climate effects in Table 6 over August 12-27 for aerosols (A), emissions (E), injection height (I) and nudging winds (W). Estimates where p < 0.05 have been bolded for clarity.

	ΔSWDS		ΔPBL		ΔT	
	Estimate	p	Estimate	p	Estimate	p
b_0	-112.3	0.000	-412.0	0.000	-3.062	0.000
b_1 (A)	**-28.6**	**0.000**	**-70.6**	**0.000**	**-0.750**	**0.000**
b_2 (E)	**9.3**	**0.000**	**22.4**	**0.002**	**0.309**	**0.000**
b_3 (I)	**-15.5**	**0.000**	**-47.8**	**0.000**	**-0.600**	**0.000**
b_4 (W)	-0.8	0.447	**-12.7**	**0.017**	0.010	0.632
b_5 (AE)	-1.7	0.138	**-16.4**	**0.006**	-0.051	0.054
b_6 (AI)	-0.8	0.466	4.7	0.250	**-0.129**	**0.002**
b_7 (AW)	-0.8	0.449	0.0	0.990	-0.024	0.300
b_8 (EI)	0.8	0.431	0.1	0.974	**0.078**	**0.013**
b_9 (EW)	1.2	0.288	0.6	0.883	0.025	0.282
b_{10} (IW)	**-4.5**	**0.006**	-7.8	0.086	**-0.095**	**0.006**

Table 8. Mean biases between observed and GFS-forecast daily maximum surface temperature (ΔT_{max}) for 10 NCEI Integrated Surface Database weather stations for the July 1- August 11 background and August 12-27, 2017 smoke plume periods. The GFS-estimated plume effect on T_{max} is the difference between the background and plume period biases.

					ΔT_{max} (ºC), Fcst-Obs		
	ID	Name	Lat	Lon	July 1 to Aug 11	Aug 12 to Aug 27	Estimated smoke effect on T_{max} (ºC)
1	711600	FORT RELIANCE (AUT) NWT	62.70	-109.15	-4.2	-1.9	-2.2
2	718740	BATHURST INLET	66.83	-108.02	-0.6	2.4	-3.0
3	713560	BAKER LAKE CLIMATE NU	64.32	-96.00	-1.0	2.9	-3.9
4	711740	ARVIAT	61.09	-94.07	-0.7	4.6	-5.3
5	710735	WHALE COVE AIRPORT	62.23	-92.60	-1.3	4.5	-5.8
6	710830	RANKIN INLET	62.81	-92.12	-1.9	3.5	-5.4
7	718429	CHESTERFIELD INLET	63.33	-90.72	0.6	2.9	-2.3
8	710490	WAGER BAY (AUT) MAN	65.87	-89.43	-1.3	2.8	-4.1
9	710944	REPULSE BAY	66.52	-86.23	-2.0	2.7	-4.7
10	719150	CORAL HARBOUR	64.19	-83.36	0.5	2.5	-2.0

Figures

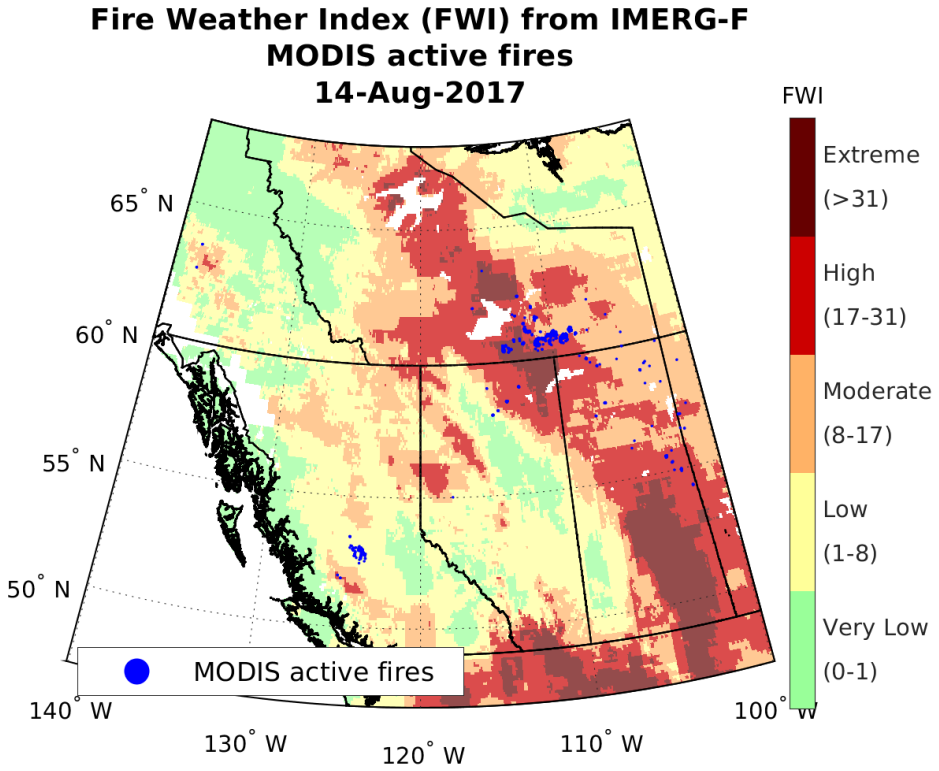

Figure 1. MODIS active fires and Fire Weather Index (FWI) on August 14, 2017, the day of peak fire activity and smoke emissions south of Great Slave Lake in the Northwest Territories. The smaller cluster of active fires in British Columbia is the remnant of the August 12 Pacific Northwest pyroCb event. The FWI is from the Global Fire Weather Database (Field, 2020), with categories from Stocks et al. (1989).

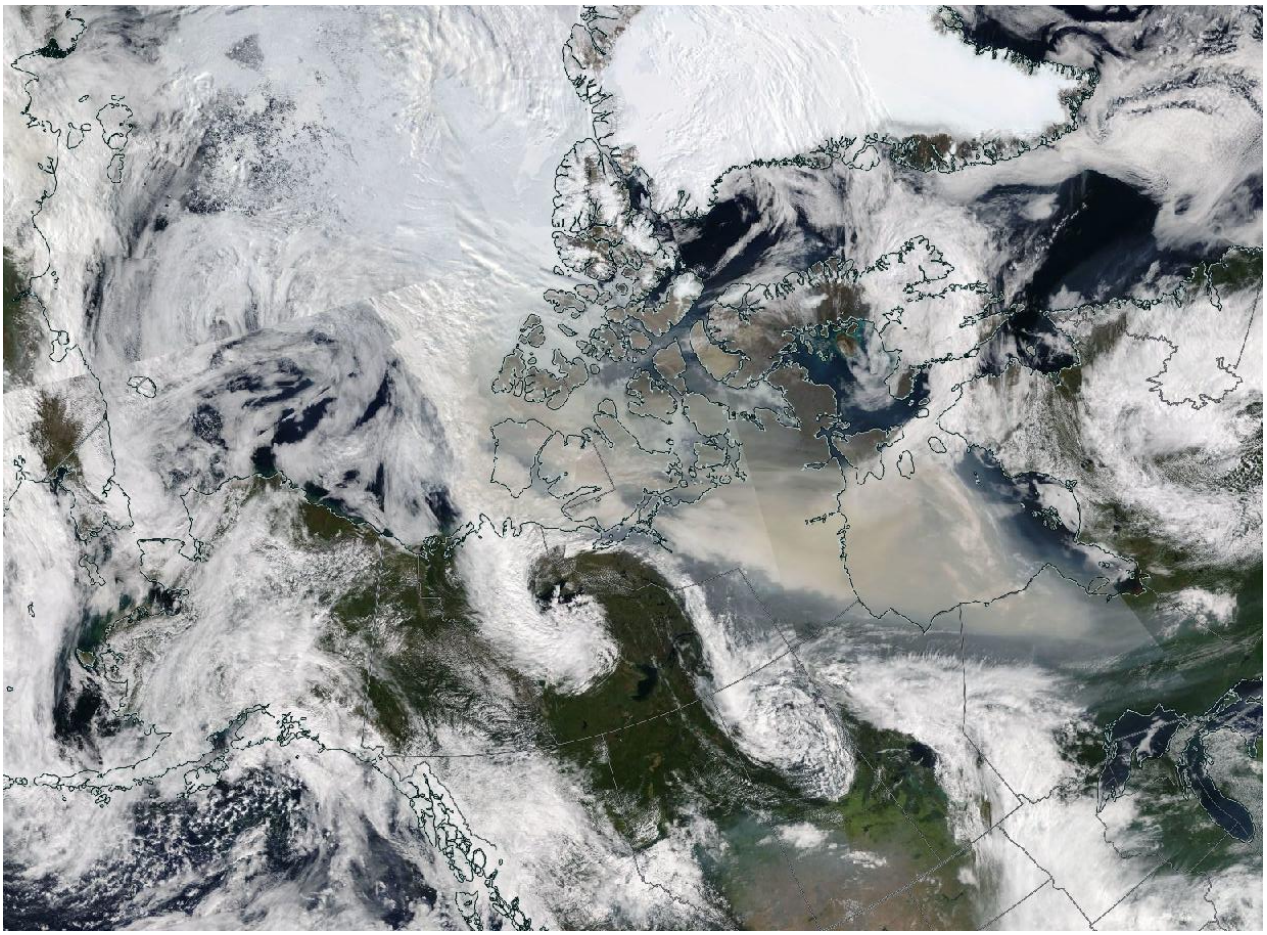

Figure 2. Terra true color MODIS image over northern Canada for August 16, 2017 from NASA Worldview. The smoke stretches 3200 km from Banks Island in the western Canadian Arctic to northern Ontario, and covered an area of ~2 900 000 km^2.

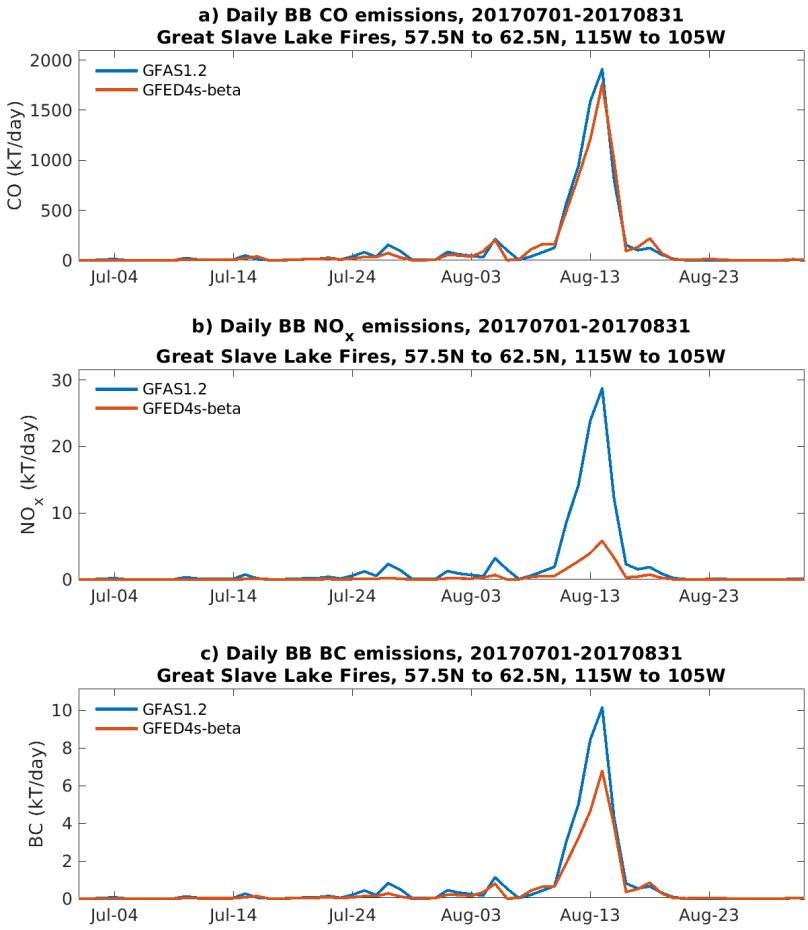

Figure 3. Daily July-August 2017 biomass burning (BB) emissions over Great Slave Lake region from GFAS and GFED for a) carbon monoxide (CO), b) nitrogen oxides (NO_x), and c) black carbon (BC). Also included in the emissions but not shown are ammonia, sulfur dioxide, methane and grouped non-methane volatile organic compounds.

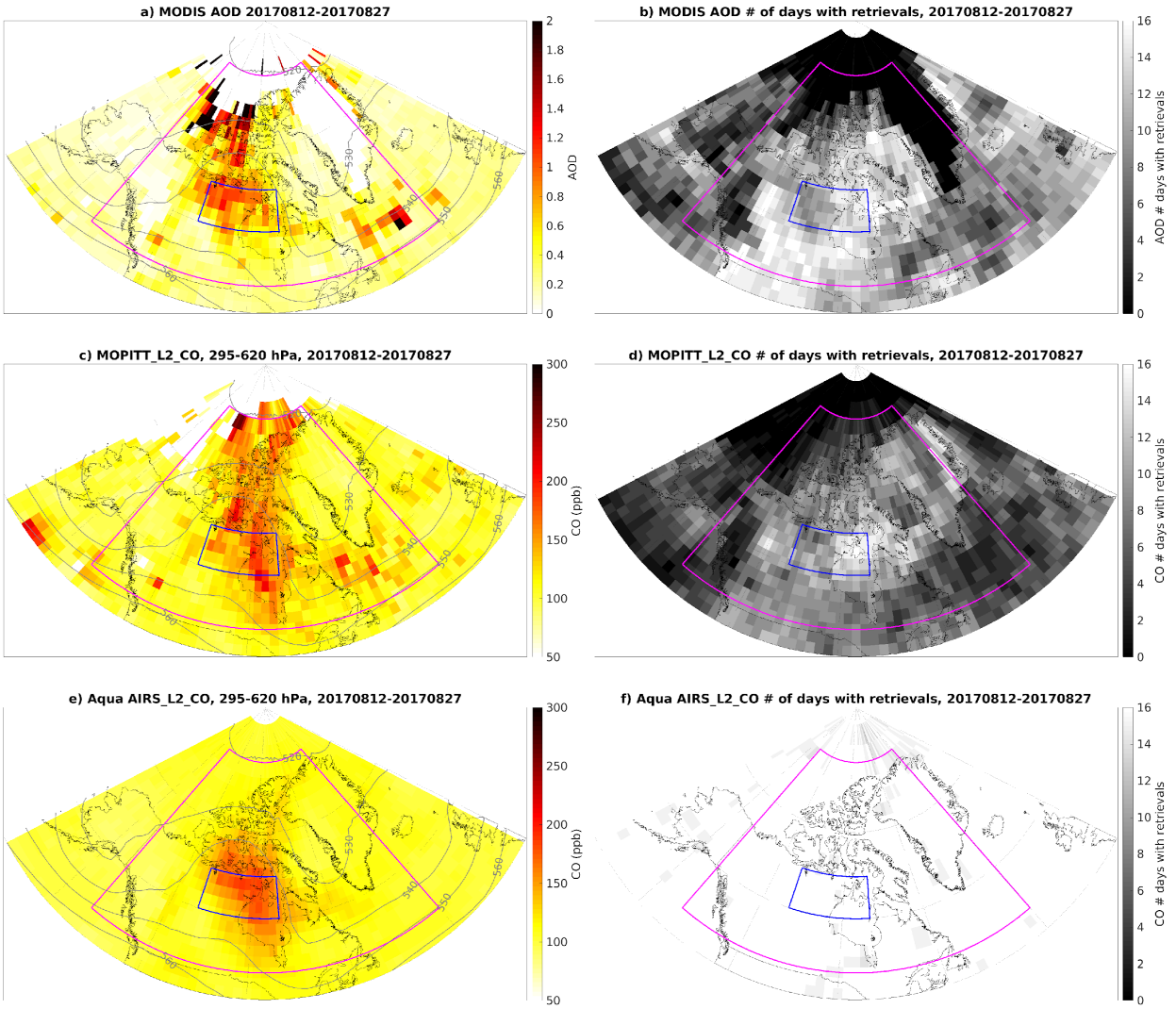

Figure 4. August 12 to 27, 2017 average a) Terra and Aqua MODIS aerosol optical depth (AOD), b) MODIS AOD retrieval counts, c) Terra MOPITT carbon monoxide (CO) over 295-620 hPa, d) MOPITT retrievals counts, e) Aqua AIRS CO averaged over 295-620 hPa, and f) AIRS retrieval counts. Geopotential height at 500 hPa (dam) is shown by the grey contours. The large analysis region over which model-satellite agreement is examined is shown by the magenta box, and the small ~850,000 km^2 analysis region over which smoke effects on land are examined is shown by the small blue box. Level 2 satellite retrievals have been averaged to the ModelE grid.

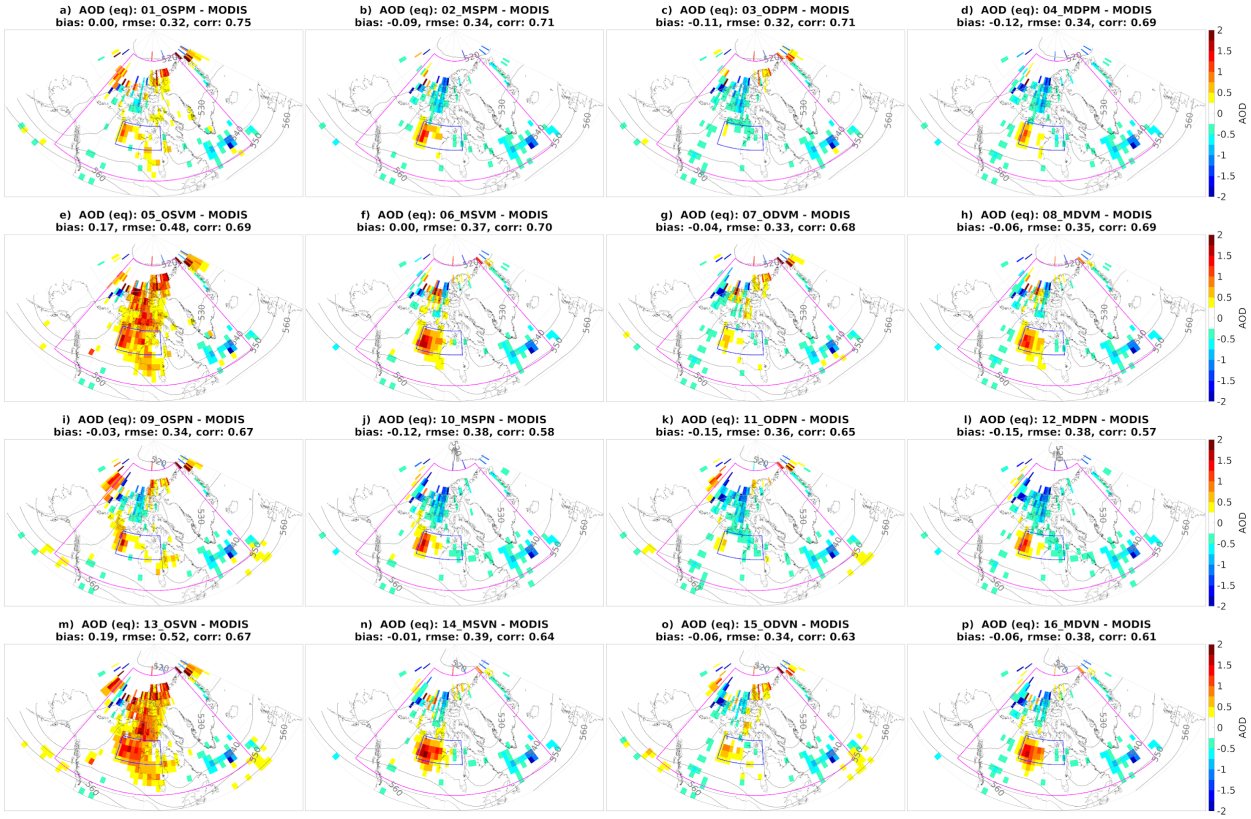

Figure 5. Difference between ModelE instrument-equivalent AOD for the 16 simulations in Table 1 and MODIS AOD averaged over August 12 to 27, 2017. The caption lists the bias, RMSE and pattern correlation between each simulation and the MODIS AOD (Figure 4a) over the region in the magenta box, and are listed for all experiments in Table 2.

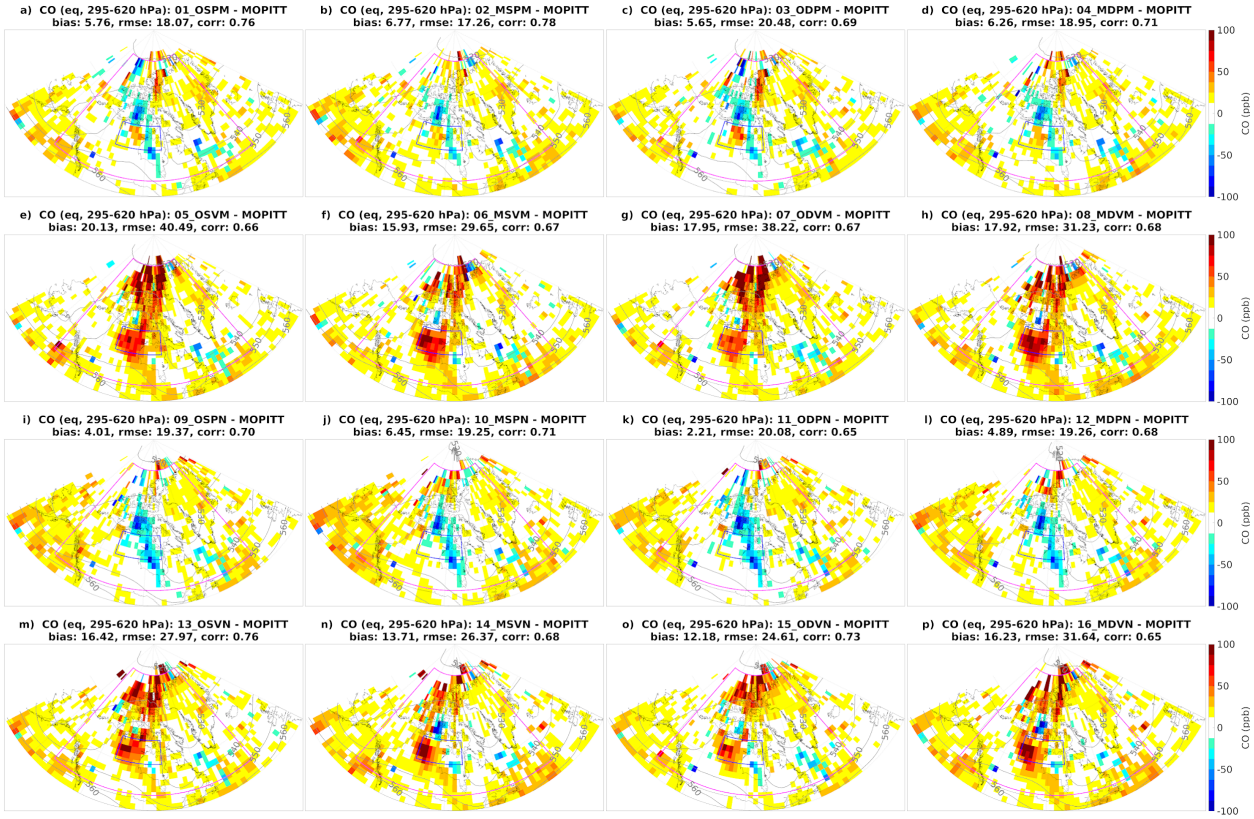

Figure 6. Same as Figure 5, but for ModelE instrument-equivalent CO and MOPITT CO in Figure 4c.

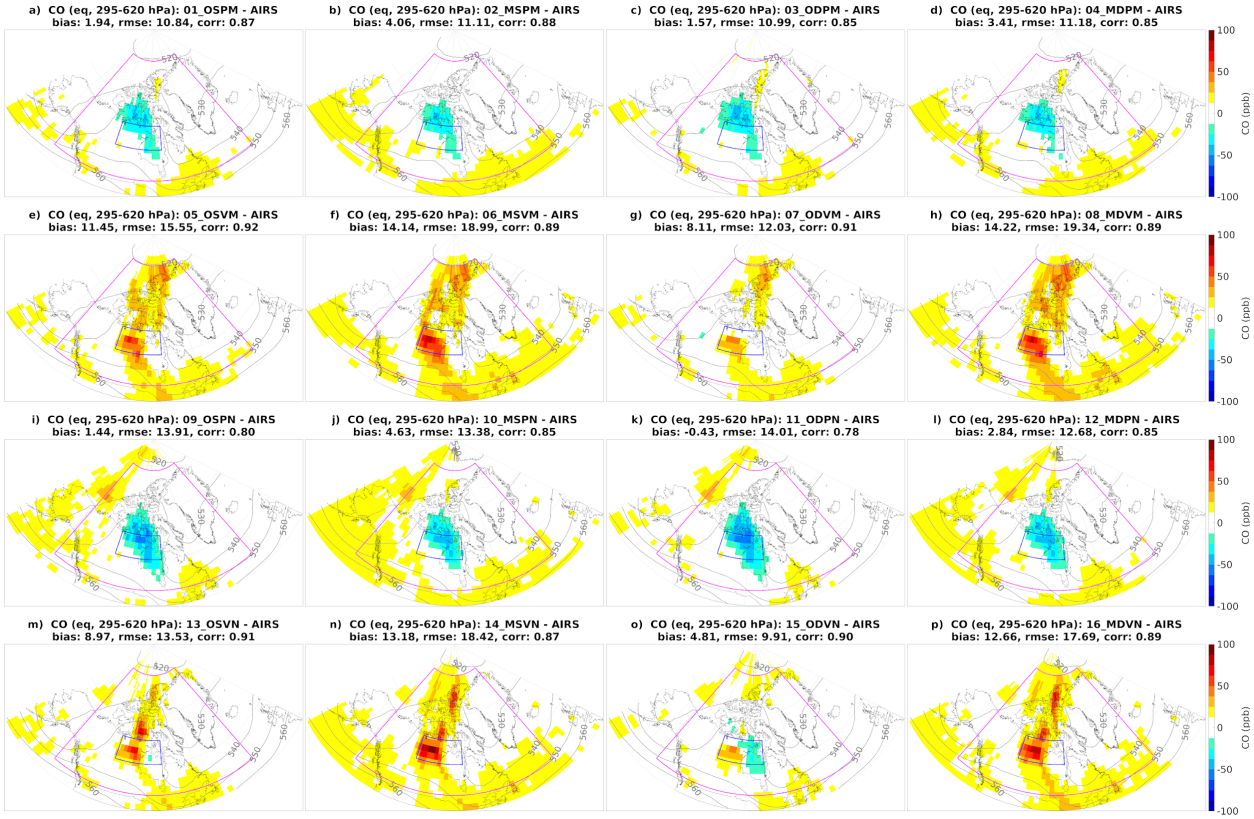

Figure 7. Same as Figure 5, but for ModelE instrument-equivalent CO and AIRS CO in Figure 4e.

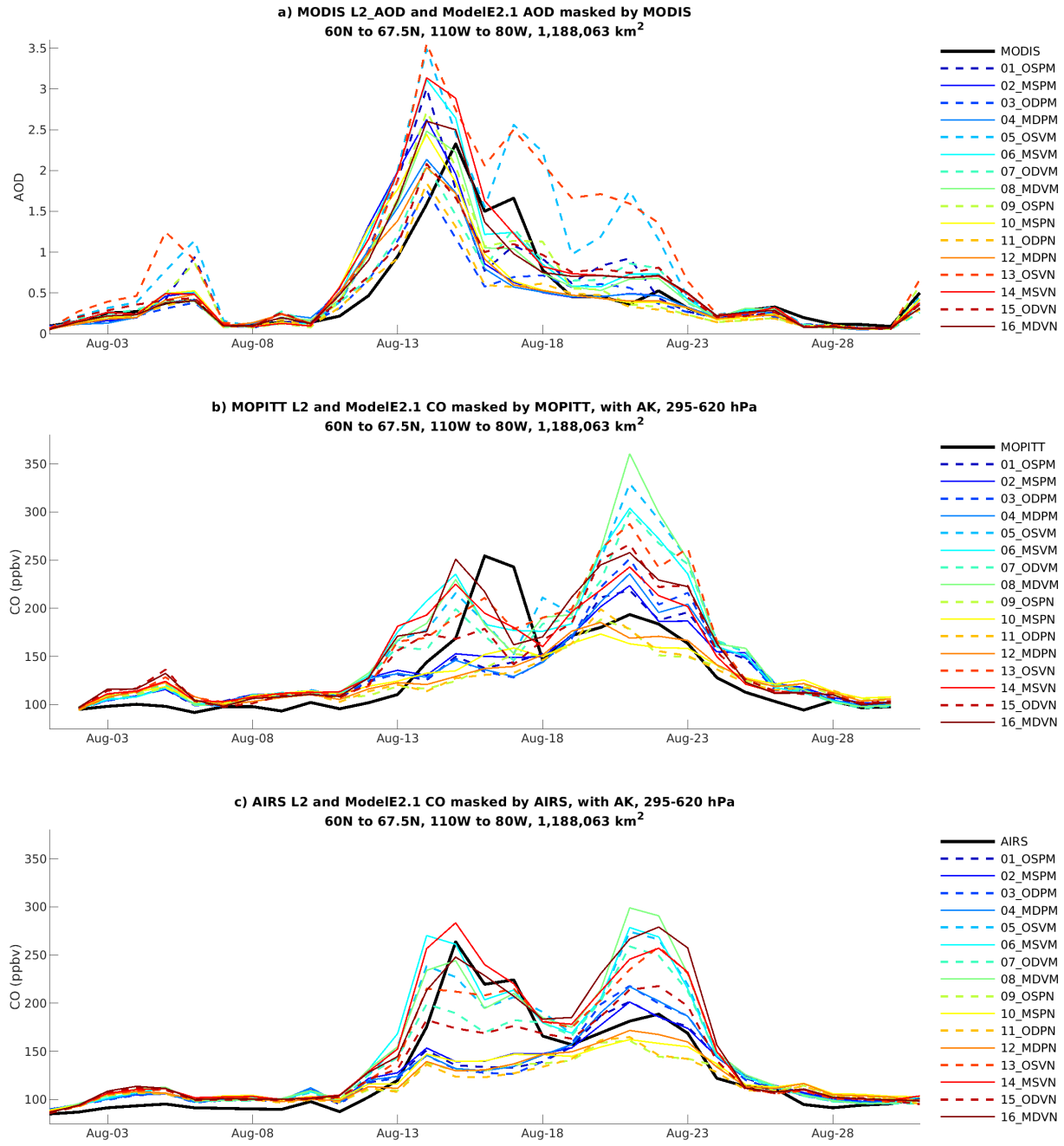

Figure 8. Time series of AOD and CO over small analysis region. All ModelE fields are instrument-equivalent estimates.

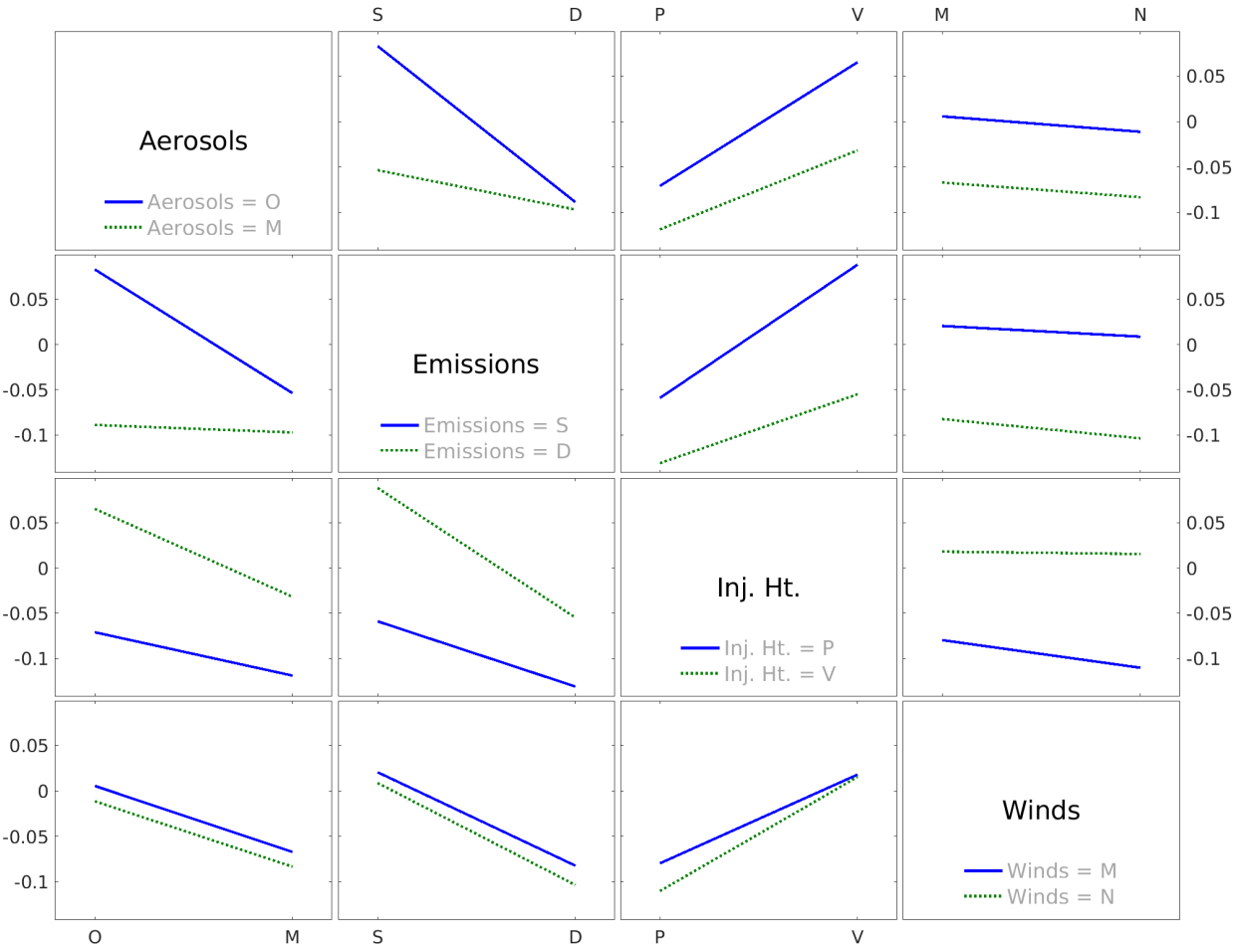

Figure 9. Interaction plot for the influence of aerosol module, emission, injection height and nudging winds on ModelE AOD bias relative to MODIS. Interactions between the factors listed in the diagonal panels can be identified by different slopes in the adjacent panels for other factors. See Montgomery (2013) for additional guidance on interpretation.

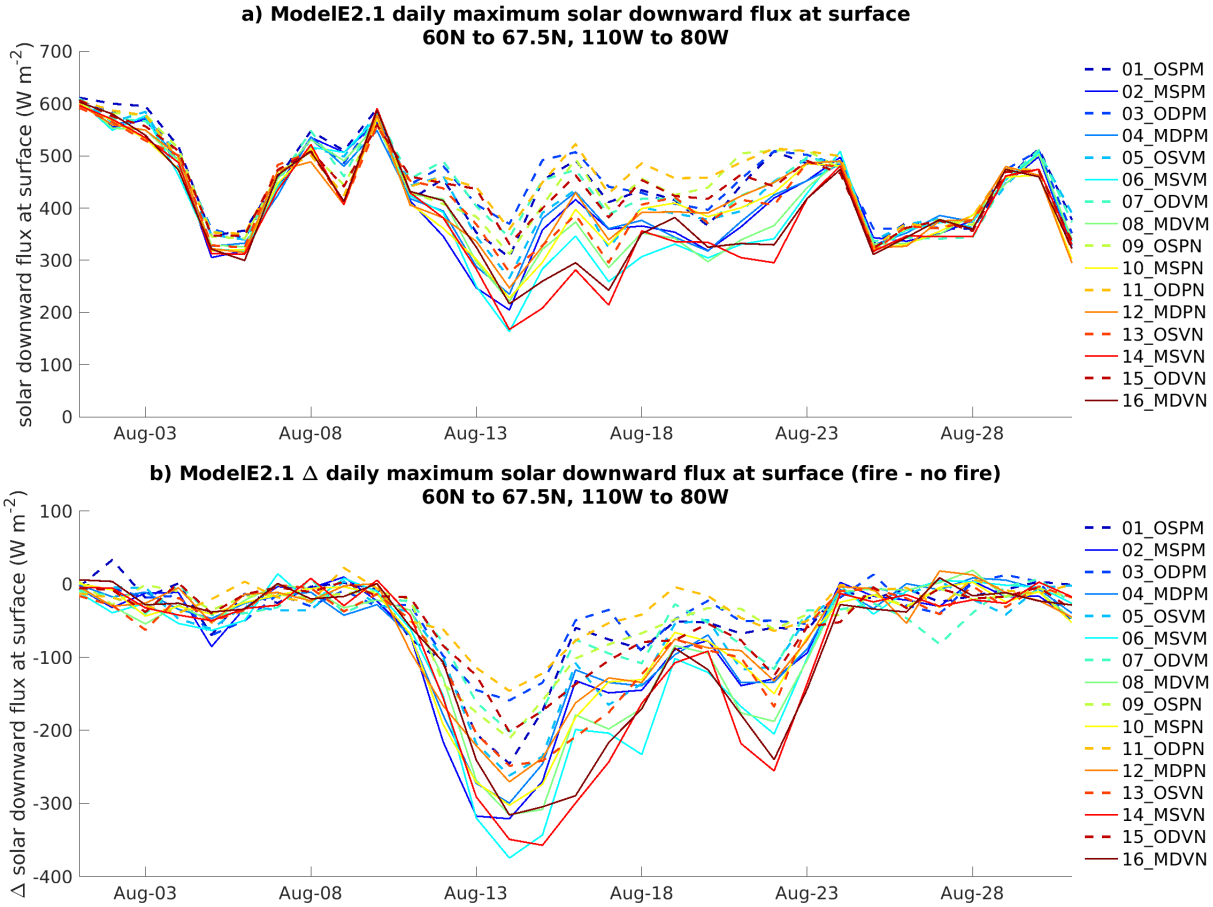

Figure 10. ModelE a) Daily maximum solar downward flux at surface over small region across all simulations with fire and b) difference between fire and no-fire experiments over the same region. Dashed lines are for experiments with OMA aerosols and solid lines are for experiments with MATRIX aerosols.

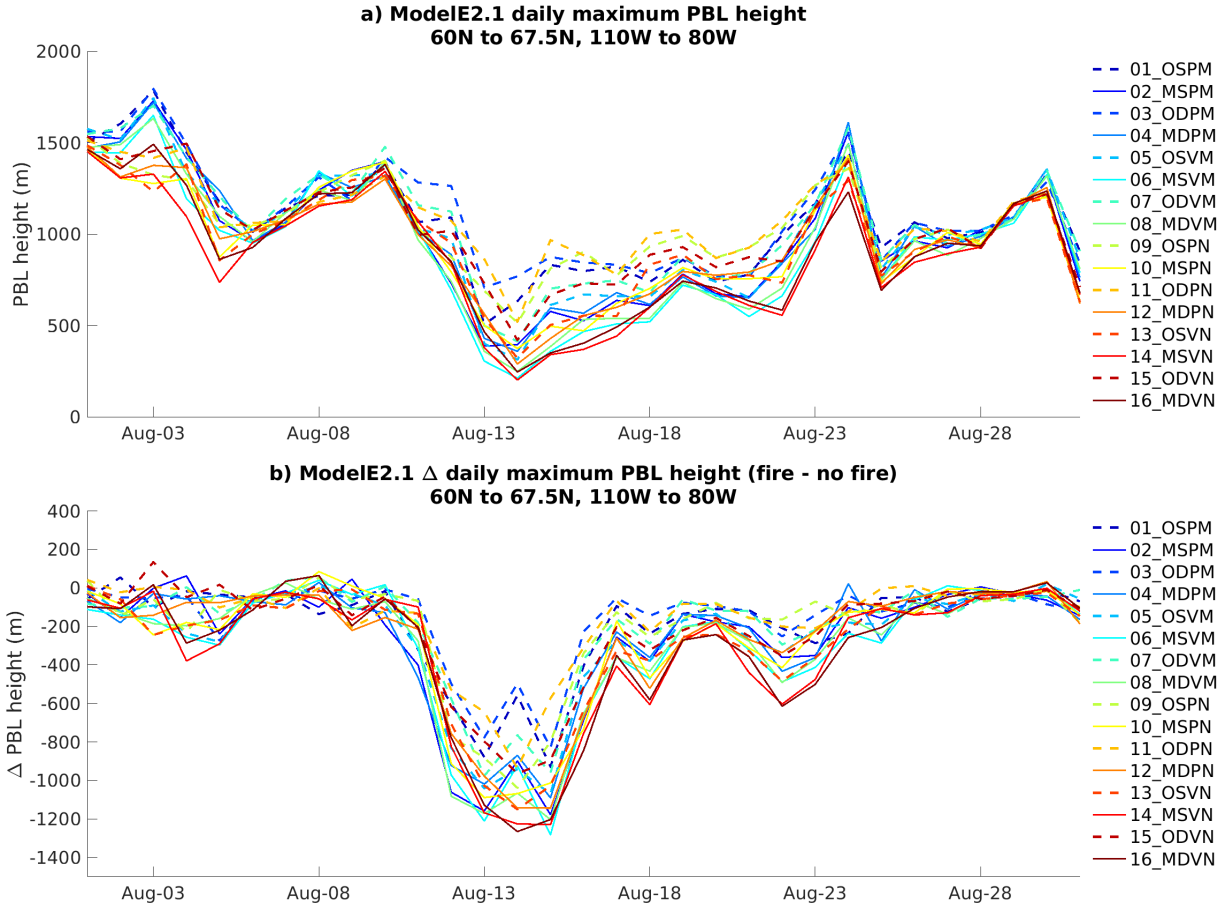

Figure 11. Same as Figure 10 but for planetary boundary layer (PBL) height.

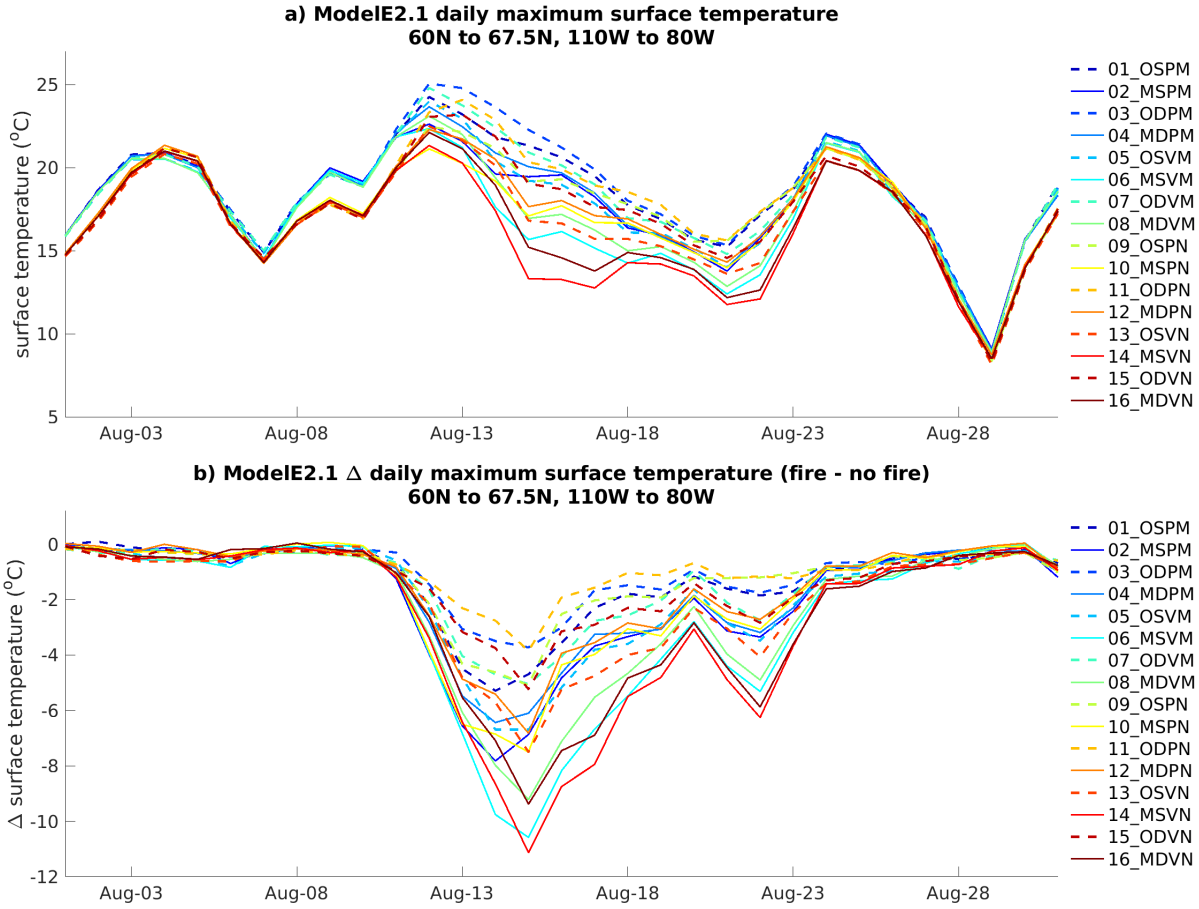

Figure 12. Same as Figure 10 but for surface temperature.

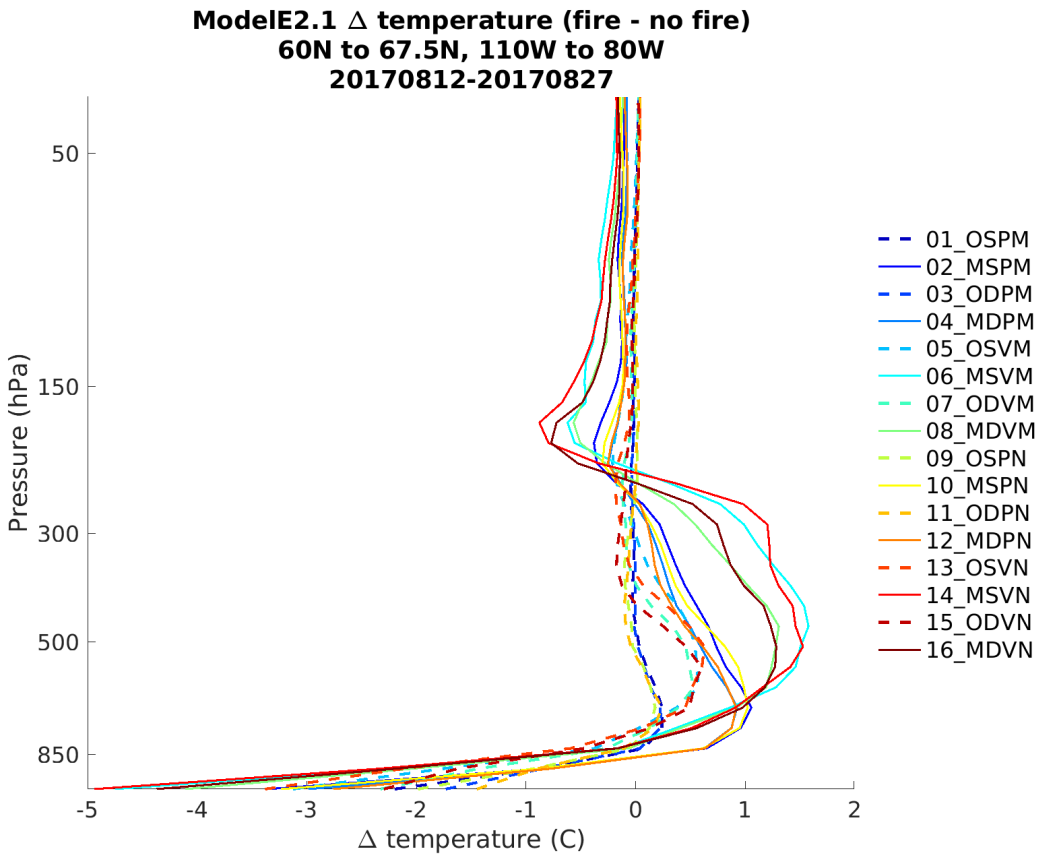

Figure 13. Average change in temperature profile over August 12-27 2017 between ModelE experiments with and without fire.

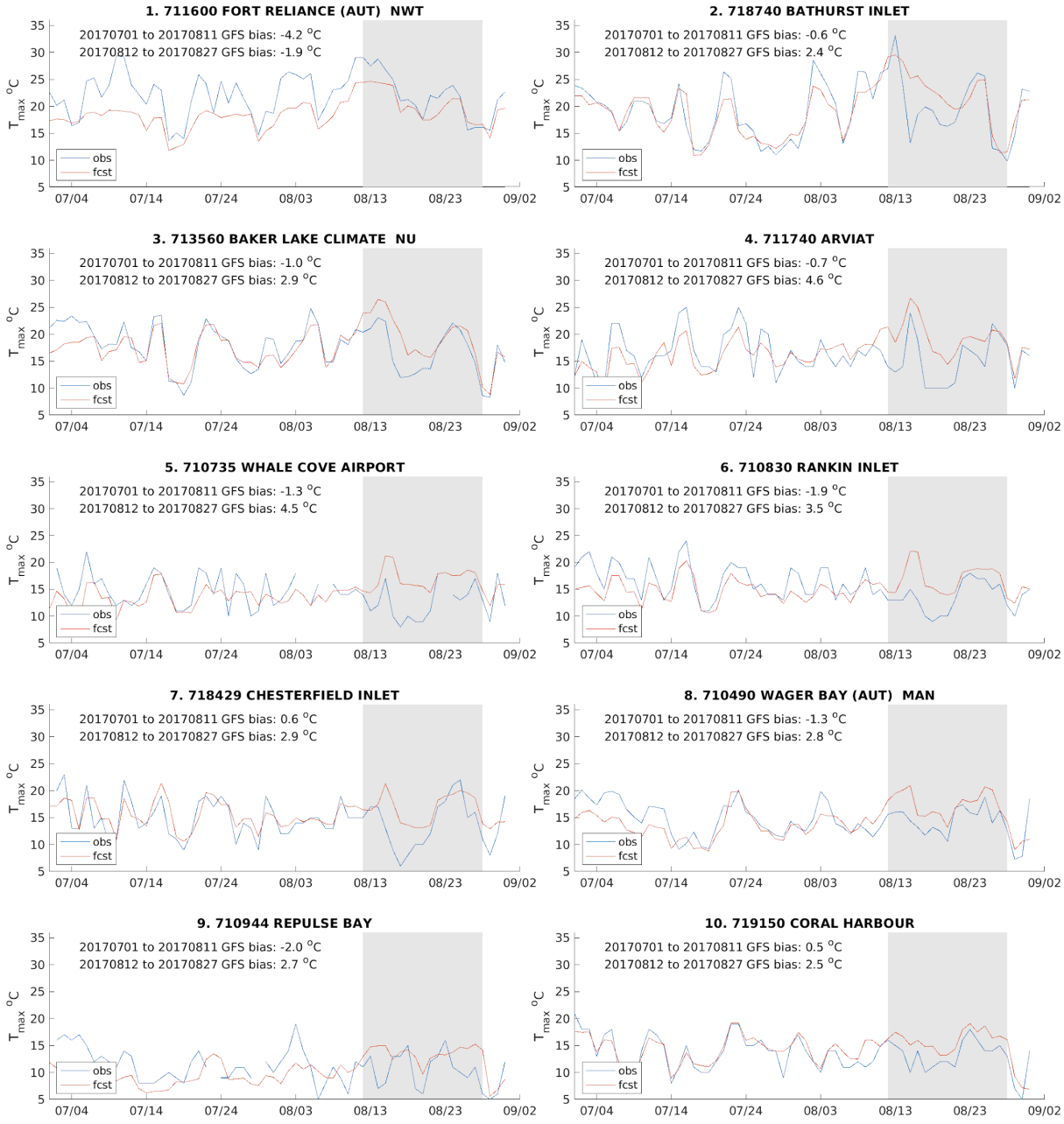

Figure 14. Observed and NCEP GFS 24-forecasts of daily maximum surface temperature at the ten stations listed in Table 8, with the average GFS bias during the July 1 to August 11 background period and the August 12-27 plume period, the latter shown by the grey shading.

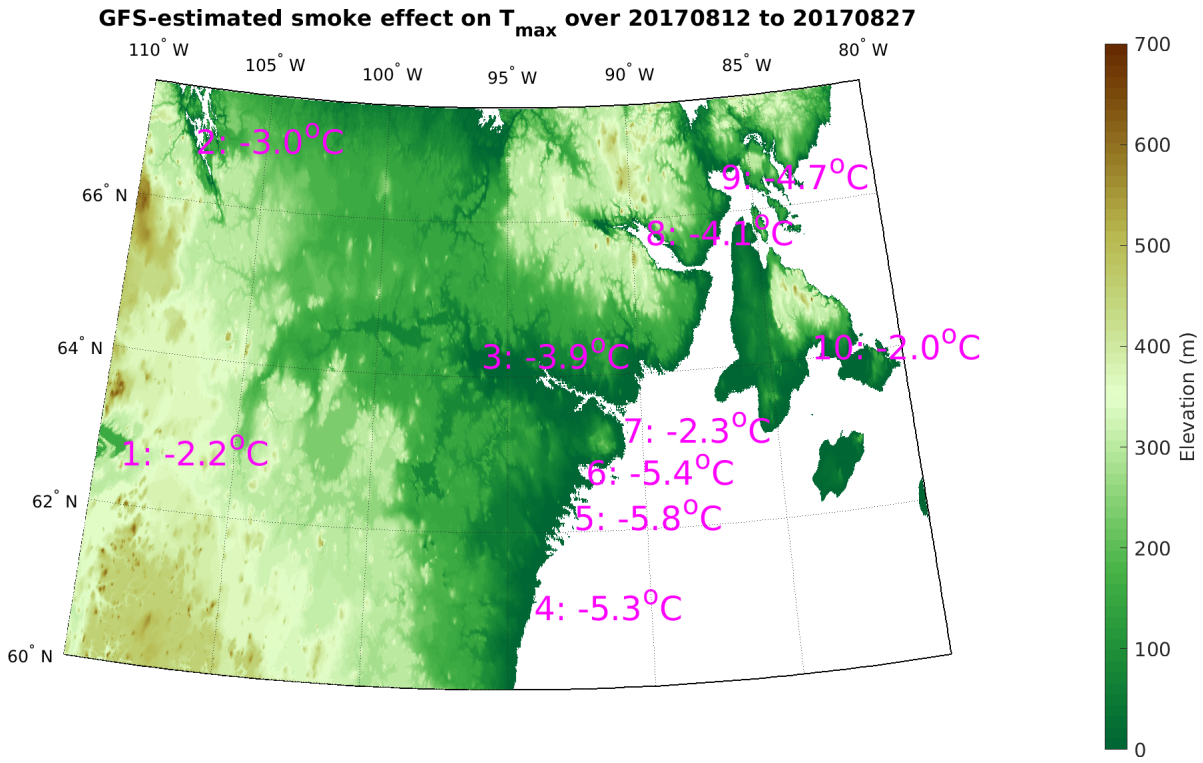

Figure 15. GFS-estimated smoke effects on surface temperature from Table 8.

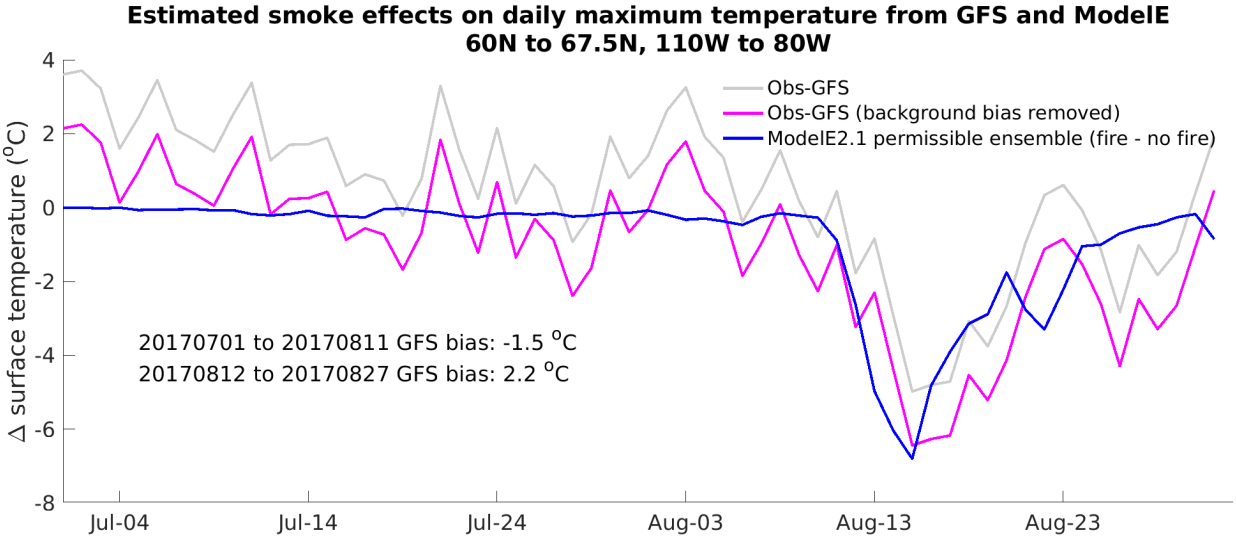

Figure 16. Daily difference between observations and GFS forecast of daily maximum surface temperature, with the ModelE fire-no-fire temperature averaged difference permissible experiments (all excluding #5 and #13). The GFS-estimated regional smoke effect on T_{max} during August 12-27 is -3.7 °C. The ModelE estimate excluding experiments 5 and 13 was -3.0 °C.

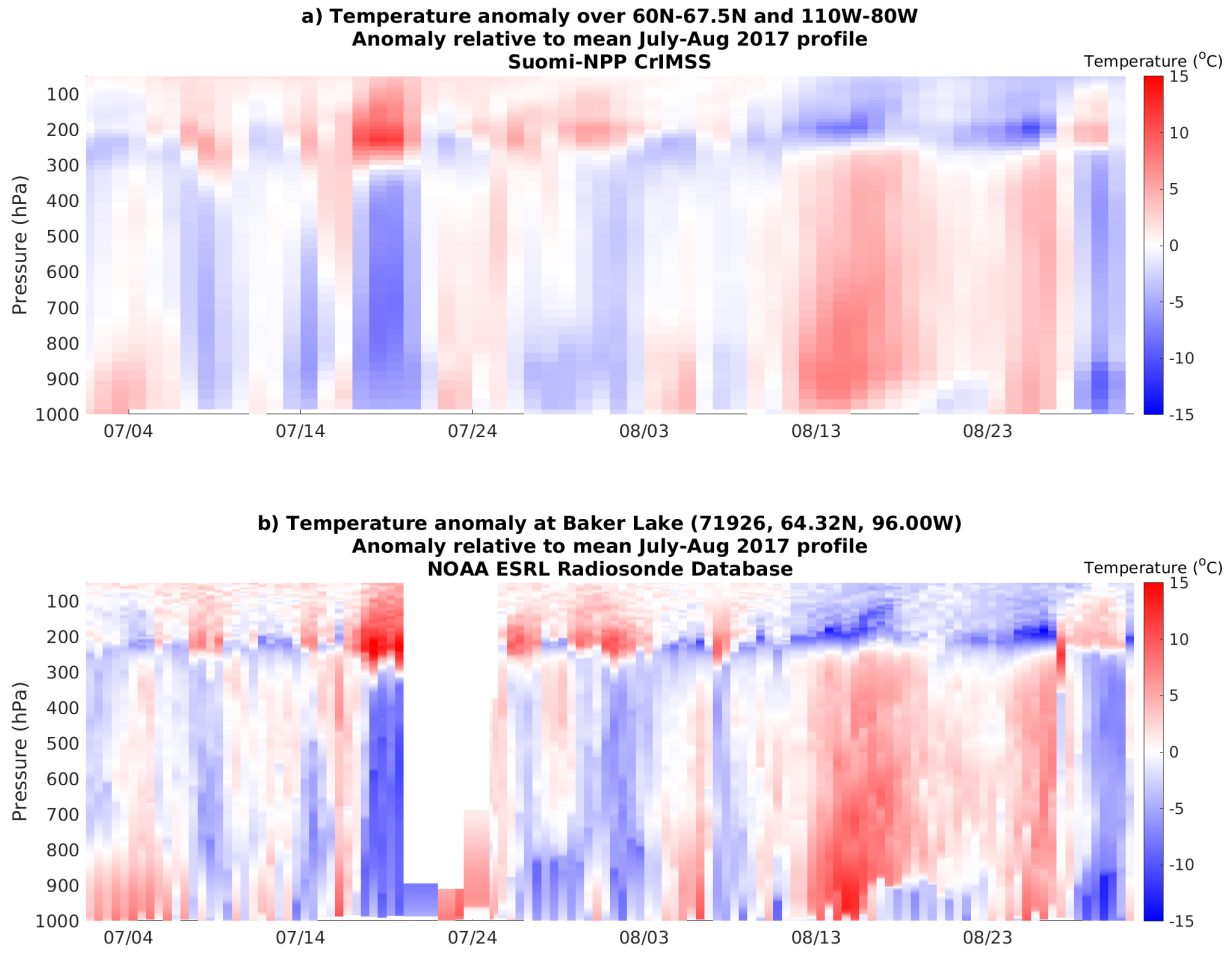

Figure 17. Vertical temperature anomalies relative to July-August 2017 mean for a) Suomi-NPP CrIMSS over the small region and b) radiosonde at Baker Lake, Nunavut, station #3 in Table 8.

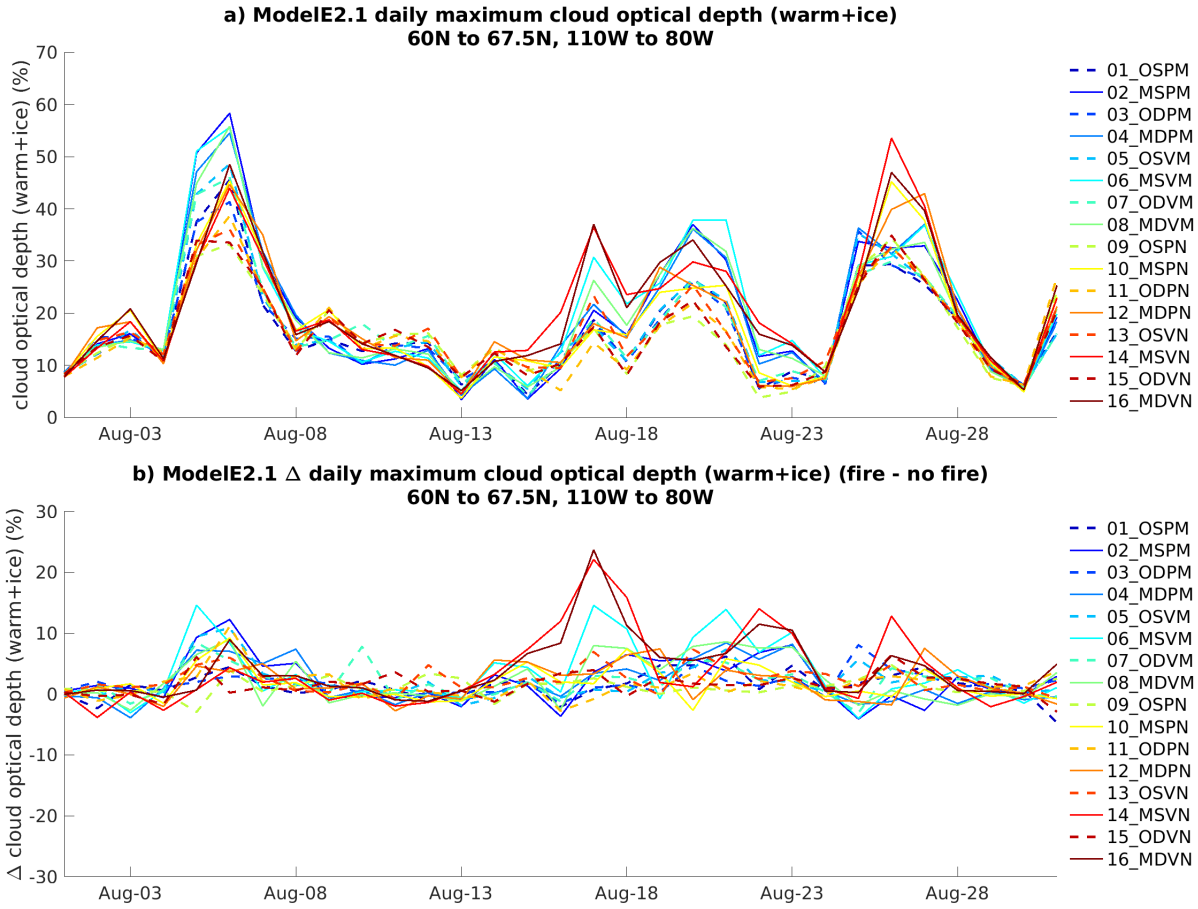

Figure 18. As in Figure 10 but for cloud optical depth.